HHS Public Access

Author manuscript

Ocul Surf. Author manuscript; available in PMC 2016 July 01.

Published in final edited form as:

Ocul Surf. 2015 July ; 13(3): 187–203. doi:10.1016/j.jtos.2015.05.002.

In vivo confocal microscopy of the cornea: New developments in image acquisition, reconstruction and analysis using the HRT-Rostock Corneal Module

W. Matthew Petroll, PhD and **Danielle M. Robertson, OD, PhD**

Department of Ophthalmology, University of Texas Southwestern Medical Center, Dallas, TX, USA.

Abstract

The optical sectioning ability of confocal microscopy allows high magnification images to be obtained from different depths within a thick tissue specimen, and is thus ideally suited to the study of intact tissue in living subjects. In vivo confocal microscopy has been used in a variety of corneal research and clinical applications since its development over 25 years ago. In this article we review the latest developments in quantitative corneal imaging with the Heidelberg Retinal Tomograph with Rostock Corneal Module (HRT-RCM). We provide an overview of the unique strengths and weaknesses of the HRT-RCM. We discuss techniques for performing 3-D imaging with the HRT-RCM, including hardware and software modifications that allow full thickness confocal microscopy through focusing (CMTF) of the cornea, which can provide quantitative measurements of corneal sublayer thicknesses, stromal cell and extracellular matrix backscatter, and depth dependent changes in corneal keratocyte density. We also review current approaches for quantitative imaging of the subbasal nerve plexus, which require a combination of advanced image acquisition and analysis procedures, including wide field mapping and 3-D reconstruction of nerve structures. The development of new hardware, software, and acquisition techniques continues to expand the number of applications of the HRT-RCM for quantitative in vivo corneal imaging at the cellular level. Knowledge of these rapidly evolving strategies should benefit corneal clinicians and basic scientists alike.

Keywords

Confocal microscopy; cornea; in vivo imaging; image analysis; three-dimensional reconstruction

Corresponding Author: W. Matthew Petroll, PhD, Department of Ophthalmology, UT Southwestern Medical Center, 5323 Harry Hines Blvd., Dallas, TX 75390-9057. Tel: 214-648-7216. Fax: 214-648-2382. matthew.petroll@utsouthwestern.edu.
Single-copy reprint requests to W. Matthew Petroll, PhD, Department of Ophthalmology, UT Southwestern Medical Center, 5323 Harry Hines Blvd., Dallas, TX 75390-9057.

The authors have no commercial or proprietary interest in any concept of product discussed in this article.

I. Introduction

Confocal microscopy provides higher resolution images with better rejection of out-of-focus information than conventional light microscopy. The optical sectioning ability of confocal microscopy allows images to be obtained from different depths within a thick tissue specimen, thereby eliminating the need for processing and sectioning procedures. Thus, confocal microscopy is uniquely suited to the study of intact tissue in living subjects. In vivo confocal microscopy has been used in a variety of corneal research and clinical applications since its development over 25 years ago. Unlike other anterior segment imaging approaches, such as high frequency ultrasound and spectral domain optical coherence tomography (**OCT**), confocal microscopy provides high-resolution en face images of corneal cells and structures. Because of this unique ability to image the cornea 4-dimensionally at the cellular level (x, y, z and t), confocal microscopy is ideally suited to monitoring the cellular events of wound healing following incisional surgery, endothelial keratoplasty,[1] corneal crosslinking procedures,[2] and refractive surgical procedures such as photorefractive keratectomy (**PRK**) and laser-assisted in situ keratomileusis (**LASIK**) (for reviews, see references 3–7).

Another important application of confocal microscopy is for the early detection and diagnosis of infectious organisms (for reviews, see references 8–10). The effects of contact lens wear on the morphology and thickness of the corneal epithelium have also been quantified, and such studies have provided important insights into how lens type and wear pattern influence bacterial binding and corneal epithelial homeostasis.[11–15] In addition, confocal microscopy has been used to monitor changes in keratocyte density during aging, in keratoconus patients, and following surgery.[16–20] As detailed in Section III, one of the most important applications of in vivo confocal imaging is the assessment of changes in the subbasal nerve plexus in response to injury or disease. Numerous other applications of this technology that are documented in the literature will not be covered here due to space limitations; many of these are discussed in several excellent review articles.[3,6,8,21–27]

Three main confocal systems have been developed for in vivo corneal imaging: the Tandem Scanning Confocal Micrscope (**TSCM**),[28–30] the Confoscan 4 (Nidek Technologies Srl, Padova, Italy),[31, 32] and the Heidelberg Retinal Tomograph with Rostock Corneal Module (**HRT-RCM**, Heidelberg Engineering, GmBH, Dossenheim, Germany [Figure 1A]).[6] The HRT-RCM is a laser scanning confocal microscope, which operates by scanning a 670 nm laser beam in a raster pattern over the field of view.[33] The system uses a high numerical aperture 63x objective lens (0.9 NA), and produces images with high contrast and better axial resolution (7.6 μm) than other in vivo confocal systems (9 μm for the TSCM and 24 μm for the Confoscan).[30,34,35]

Normal human corneal anatomy as observed with the HRT-RCM is shown in Figure 2.[21] Confocal images are always taken en face; that is, the viewer sees thin slices of the cornea that are parallel to the epithelial surface. An inductive displacement transducer is used to measure the position of the objective lens, and the position of the focal plane is continuously displayed on the personal computer (**PC**) software interface during scanning. Due to the

axial resolution of HRT-RCM, intraepithelial sectioning can be achieved, and wing cells (Figure 2A) and basal cells (Figure 2B) can be easily distinguished.

Langerhans cells can also be identified and their density quantified using the HRT-RCM microscope (not shown).[26] Immediately beneath the basal epithelium, a fine nerve plexus can be detected (Figure 2C). In the corneal stroma, only cell nuclei are visible under normal conditions, with a dark background in between (Figure2D and 2E). As detailed in Section II.B., depth-dependent changes in keratocyte density can be assessed using confocal imaging. Large numbers of keratocytes are present in the anterior stroma just under Bowman's layer in the human, as compared to the middle and deeper stroma, which show a progressively lower cell density.[24] Interestingly, the interconnected cell processes of the keratocytes become visible under certain pathologic conditions, due to tissue edema, cell activation and/or decreased expession of corneal crystalline proteins.[36] Images of the normal endothelium appear similar to what is observed using specular microscopy (Figure 2F), and endothelial cell density and morphology can be quantified.[26,27]

In addition to collecting 2-dimensional (**D**) images of corneal cell layers, automated z-scans of approximately 80 μm (40 images with a 2 μm step size) can be generated with the HRT-RCM using a motorized internal lens drive. These "volume scans" have been used to produce 3-D reconstructions of the corneal epithelium in the human, and the corneal stroma in the mouse.[2,37,38] However, to change the focal plane over larger distances, a manual thumbscrew drive is used, which requires rotating the objective housing by hand (Figure 1A, arrow). Custom, motorized drive systems have been added by individual users to allow hands-free focusing of the instrument, which eases the examination process.[35,39] As described in Section II, when combined with specialized acquisition and analysis software, such modifications can allow quantitative 3-D imaging of the full thickness cornea.

The HRT-RCM uses a flat applanating tip (Tomocap) to provide z-axis stability during imaging. One drawback of the flat tip is that compression artifacts are sometimes produced, which can distort cellular structures. In addition, the reflection from the Tomocap can obscure images of the superficial epithelial cells. Zhivov et al reported that a thin PMMA washer can be placed on the Tomocap to eliminate these reflections and reduce compression artifacts; however, this technique is not routinely implemented.[35] Another factor that can impair quantitative image analysis is excessive movement of the patient or animal during scanning. Movement during a raster scan results in stretching and distortion of corneal cells in the digitized image.[27] Thus, it is important to identify images that were collected while the cornea was stable and exclude the others from quantitative image analysis.

The HRT-RCM provides the highest quality images of the cornea in terms of resolution, contrast and signal-to-noise ratio (**SNR**), which has led to the expansion of its development and use in recent years. In this article, we review the latest developments in instrumentation, acquisition techniques, and quantitative analysis procedures for the HRT-RCM. We discuss hardware and software modifications that allow full thickness 3-D imaging of the cornea, thereby allowing quantitative measurements of corneal sub-layer thicknesses, stromal haze, and depth-dependent changes in corneal keratocyte density to be obtained. We also review current approaches for imaging and characterizing the subbasal nerve plexus, including 2-D

morphometric analyses, wide-field mapping, and 3-D reconstruction of nerve structures. Such advances in imaging technologies and processing techniques should continue to expand the potential applications of the HRT-RCM for in vivo corneal imaging.

II. Full-Thickness 3-D Corneal Imaging and Analysis

A. Confocal Microscopy Through-Focusing (CMTF) with the HRT-RCM

To collect and quantify 3-D information from the cornea, a technique termed *confocal microscopy through-focusing* (**CMTF**) was developed for the TSCM by Jester and coworkers.[40,41] This technique is based on the observation that different corneal sub-layers generate different reflective intensities when imaged using confocal microscopy.[42] CMTF scans are obtained by scanning through the cornea from the epithelium to endothelium at a constant lens speed, while continuously acquiring images. As mentioned above, changing the focal plane with the HRT–RCM is normally accomplished using a thumbscrew drive which is rotated by hand (Figure 1A). Because CMTF imaging requires continuous focal plane movement at a known speed, *quantitative* high-resolution 3-D imaging of the full-thickness cornea is not possible with the standard HRT-RCM system. In a recent study, however, the HRT-RCM hardware and software were modified to address this limitation and allow quantitative CMTF imaging.[43]

First, the thumbscrew drive was removed to allow the front assembly of the microscope to move freely. A Newport TRA25CC Motorized Actuator with DC Servo motor drive enclosed in a custom-made housing was then attached to the HRT scan head (Figure 1B). The actuator was coupled to the front section of the microscope, using a spring-loaded drive shaft. This rigid assembly ensured proper alignment of the motor drive shaft with the z-axis of the HRT-RCM. Initially, the existing CMTF program was modified to control the position of the Newport motor via a serial interface to a Newport Single Axis Motion Controller (SMC100CC), which is connected to the TRA25CC actuator. Alternatively, a joystick remote can be used with a more expensive controller (Newport ESP301-1N), which eliminates the need for a second PC. In theory, a rotational motor drive could be used to rotate the thumbscrew housing, thus simplifying the hardware interface. In pilot studies, however, it was found that there are variations in the relationship between rotational speed and focal plane movement during the course of a 360-degree rotation of the housing (unpublished observation), suggesting that the tolerances of the thumbscrew mechanism are not sufficient for performing high-resolution 3-D scanning.

The standard HRT software collects only 100 images during a sequential acquire, which results in a large step size (>5 μm) between images in a CMTF stack of the full thickness cornea.[39] However, beta software from Heidelberg Engineering allows real-time “streaming” of images to the hard drive during an examination. With this software, much larger sequences can be obtained (maximum 14,525 images). All images in a sequence are combined into a single “.vol” file, in which each image contains a 384-byte header followed by the 384 × 384-pixel data. The CMTF software was modified so that the HRT “.vol” files could be directly loaded. The header information from each image was also decoded to determine its exact time of acquisition, and its relative z-position was then calculated based on the known scan speed (distance = velocity × time).

The modified CMTF program interface for the HRT-RCM is shown in Figure 3. The CMTF software reads and displays the image stacks, and the intensity vs depth curve is calculated and plotted on the right side of the window. It is important to note that CMTF imaging is performed with the "automatic brightness" setting in the HRT-RCM software turned off. The intensity curves obtained with the HRTRCM have the same characteristic shape as those obtained previously in the rabbit cornea with the TSCM, with three peaks corresponding to the superficial epithelium (**Epi**), basal lamina (**BL**), and the endothelium (**Endo**).[40] Note that the subbasal nerves are not generally visible in the rabbit.[44] The CMTF program also generates side views of the image stack (x–z and y–z slices) and a 3-D surface projection.[41] Updating these views occurs dynamically; that is, the user can interactively pick a region of interest by dragging the corners of a highlighted "region of interest" box in the *x–y* plane, while the side views and the 3-D projection are continuously updated. This gives the user the ability to visualize and localize a structure inside the cornea interactively.

1. Assessment of Corneal Sub-layer Thickness—After the CMTF image stack has been loaded into the program, a cursor can be moved along the intensity curve as corresponding images are displayed. In this way, the user can identify images of interest and record their exact z-axis depth.[40,41] By measuring the distance between the peaks in the intensity profile corresponding to each cell layer, measurements of corneal, epithelial and stromal thickness can be obtained.[40] Rabbit corneal thickness measurements reported with the modified HRT-RCM were in good agreement with those obtained using ultrasonic pachymetry (373 ± 25 μm vs 374 ± 17 μm, respectively). However, the coefficients of variation obtained for repeated scans of the epithelium and cornea were higher than that previously reported using the TSCM system (8.2% and 2.1% versus 2.5% and 0.7%).[40] This is most likely due to the different mechanisms used for changing the focal plane on these two systems. In the TSCM, the focal plane position is changed by moving lenses inside the objective casing; thus, the tip of the objective remains stationary during scanning. In contrast, changing the focal plane position of the HRT requires movement of the Tomocap, which is in contact with the cornea. Essentially, the cornea is moved through the stationary focal plane of the objective. This movement can potentially change the degree of applanation during a scan, as well as introduce backlash when changing directions. Thus, it is important that HRT-RCM CMTF scans are made with Tomocap moving forward (which produces an image sequence from endothelium to epithelium) to ensure that the tip remains in contact with the corneal surface throughout the procedure. If the force of applanation is large, compression artifacts such as ridges and folds can be induced; these could also affect the accuracy and reproducibility of the sub-layer thickness measurements.

In addition to its use in study of the rabbit, CMTF scanning with the HRT-RCM has been successfully applied to the mouse cornea. A recent study investigated systematic changes in corneal thickness and corneal nerve morphology using 3D imaging in vivo and in situ in a streptozotocin-induced diabetic mouse model.[45] Significant thinning of both the corneal epithelium and stroma was measured in the diabetic mice using CMTF with the HRT-RCM. It should be noted that other techniques such as high-frequency ultrasound and spectral domain OCT can also provide accurate measurements of corneal sub-layer thicknesses.[46–48] However, quantitative 3-D confocal microscopy also provides a series of high-resolution en

face images which allow assessment of depth-dependent changes in cell morphology, density, and reflectivity to be evaluated.[3–5,36]

2. Assessment of Stromal Haze—One important measurement that can be made using CMTF imaging is the relative amount of stromal cell and extracellular matrix (**ECM**) backscatter (haze). In general, stromal haze is estimated by calculating the area under the CMTF intensity curve within the corneal stroma. An example is shown in Figure 4, where stromal haze is assessed in the mouse model following mechanical debridement (**MD**) injury with removal of basement membrane, as well as transcorneal freeze injury (**FI**).[49–52] MD in the mouse induces fibrosis both within and on top of the injured stroma, similar to PRK (Figure 4B).[52] FI in the mouse results in cell loss throughout the full thickness of the cornea, and also induces stromal keratocyte activation (Figure 4C).[49,50] In both injury models, an increase in cell and ECM backscattering in the cornea is identified (shaded areas under curves, “area” on top right of each image) as compared to a preoperative scan (Figure 4A) taken with the same “gain” setting (same position of horizontal slider under “image quality” readout on HRT-RCM software screen).[53–57] The HRT-RCM has also been used for quantitative assessment of stromal cell and ECM backscattering following transcorneal freeze injury in the rabbit cornea, with similar findings.[58]

Haze is expressed in arbitrary confocal backscatter units (**CBU**), defined as μm × pixel intensity. This measurement incorporates all factors that might contribute to interface backscatter, such as keratocyte activation, edema, and fibrosis. While this approach is able to show relative changes in backscatter using a single instrument using a single gain setting on the detector, the data cannot be directly compared with measurements from multiple laboratories or clinics, or taken using different gain settings. In order to overcome this limitation, measurements can be calibrated by scanning Amco Clear (GSF Chemicals, Columbus, OH), a suspended polymer solution that is commonly used to standardize measurements of scatter and turbidity.[26,27,59]

An important application of CMTF imaging has been in the assessment of the effects of refractive surgical procedures such as PRK and LASIK, in which quantitative measurements of sub-layer thickness (including flap and bed thickness) and depth-dependent cell and ECM backscatter are important.[16,56,57,60–62] CMTF has also been used to quantify corneal light scattering profile in transgenic mouse models with altered corneal clarity,[63] and to assess the effects of ocular irritants on the rabbit cornea.[64–66] The effects of contact lens wear on the thickness of the corneal epithelium has also been quantified, and such studies have provided important insights into how lens type, wear pattern, and cleaning solutions affect corneal epithelial homeostasis.[11–15] Overall, CMTF imaging can be used whenever quantitative 3-D corneal imaging is needed; additional applications are reviewed elsewhere.[3,6,7,26]

B. 3-D Assessment of Corneal Keratocyte Density

Another important application of 3-D corneal imaging is in the assessment of changes in corneal keratocyte density. The TSCM has been used to monitor changes in keratocyte density during aging, in keratoconus patients and following refractive surgery.[16–20,27] Previous studies have identified significant decreases in cell density that could potentially

have long-term clinical implications. In most studies, cell density was estimated from single (2-D) images collected at different depths from within the cornea. Since stromal cell density varies with depth in the cornea, it is critical that the z-axis position of the focal plane is calibrated when such assessments are performed. CMTF scanning is ideally suited for this purpose. Both manual and automated methods for quantifying keratocyte density have been published.[17,67] With the TSCM, image contrast is low, and distinguishing keratocytes can sometimes be difficult, particularly when automated segmentation techniques are used.

In a recent study, 3-D keratocyte density was assessed using the HRT-RCM in a rabbit model.[43] In this study, the entire CMTF dataset was used, so that the true 3-D position of each cell could be determined. In order to perform true 3-D cell counting, the images within the stack were registered to compensate for translational movement of the cornea that occurred during scanning. Specifically, the stromal images in the 3-D CMTF datasets were automatically aligned using the *linear stack alignment* plug-in in Image J (Fiji version, http://fiji.sc/Fiji), which uses features extracted via the *scale invariant feature transform* (**SIFT**). Since this alignment produces vacant areas at the edges of the shifted images, a central 200 × 200 pixel region was used for analysis. Scans with large amounts of movement had to be excluded. Manual counts of keratocyte nuclei were performed using an approach previously described by us, in which each nuclei is marked only on the image in which it is brightest.[68] As shown in Figure 5, there was the expected gradual decrease in keratocyte density from the anterior to posterior cornea (R=0.992), consistent with previous data generated in vitro.[68,69] To test the measurements, in vivo and in vitro, cell density measurements were directly compared, and no significant difference was found (39,392+652 cells/mm^3 vs. 40,781±1,526 cells/mm^3, P=.22, N = 3 scans each). Although this study used manual cell counting, the HRT-RCM should be well suited for previously published automated cell counting approaches due to the high image contrast of the stromal cell nuclei.[17,67]

C. Volume Rendering

In addition to the interactive visualization provided by the CMTF program, 3-D renderings of CMTF image stacks from the rabbit cornea have been generated using Imaris software.[43] Stacks were first loaded into Metamorph and saved as multi-image TIF files. These TIF files were read into Imaris, and a median filter was applied to remove background noise. Images were cropped in 3-D to focus on a region of interest, and rendered using an orthogonal maximum intensity projection within the *Surpass* module of Imaris. Movies showing reconstructions over a range of projection angles were generated using the *Animation* module. In one rabbit, there was minimal x–y movement of the cornea during the scanning process (maximum drift of less than 10 microns), and the reconstruction was made without aligning the images within the stack (Figure 6A). By rotating the projection angles to create a 3-D movie, the 3-D relationships between the cells and cell layers within the tissue were clearly demonstrated. A second reconstruction of the stroma of a different cornea is shown in Figure 6B. Because there was more x–y movement of the cornea during this scan (a maximum drift of 78 μm), the planes within the stack were registered prior to performing the reconstruction.

It should be noted that such reconstructions would be more difficult in the human cornea, due to involuntary eye movements that occur during scanning. Such movements can cause distortions within individual images[27] and therefore require more complex image registration techniques, as discussed in Section III.C below.[38] It should also be noted that the HRT streaming software used in this study was a beta version that is not yet FDA-approved for human use. Without this software, only 100 frames can be acquired during a sequential acquire, which is not sufficient for high-resolution 3-D reconstructions of the tissue.

III. Quantitative Imaging of the Subbasal Nerve Plexus

The cornea is one of the most highly innervated tissues in the body.[70] Corneal nerves provide trophic support to the corneal epithelium and are essential for maintaining tissue integrity and corneal health. Corneal nerves arise from the ophthalmic division of the trigeminal nerve. Upon entering the peripheral cornea, stromal nerves branch anteriorly, piercing Bowman's membrane in the human (most animals do not have a Bowman's membrane). Here they then turn and run just beneath the corneal epithelium, in a course parallel to the corneal surface. Within this subepithelial space, nerve fibers form a complex array of branching and anastomosing fibers, known as the subbasal nerve plexus (**SBNP**).[71] Terminal nerve fibers branching from the SBNP run throughout the corneal epithelium, terminating in the superficial corneal epithelial cell layers.[45] Immunohistochemical studies using ex vivo human and animal tissue have provided significant insight into the architecture of the SBNP and associated terminal nerve fibers (Figure 7).[45,70,72,73] These techniques, however, have limited usefulness in a clinical setting.

An important feature of in vivo confocal microscopy is the ability to obtain high-resolution images of the subbasal nerve plexus, particularly with the HRT-RCM (Figure 2C). Several studies have used confocal microscopy to assess temporal changes in the density and organization of subbasal nerves in response to surgery or disease.[38–40] While the SBNP is highly dynamic and undergoes centripetal migration through the cornea, it has been shown in longitudinal studies that the SBNP is sufficiently stable to allow major landmarks to be repeatedly identified over time, which is important for disease monitoring.[74] It should be noted that IVCM does not have the resolution to permit viewing of the small terminal nerve fibers within the corneal epithelium. This may explain why many studies have shown poor correlations between loss of the SBNP and a decline in corneal sensitivity. There are no studies directly comparing changes in the SBNP in vivo with ex vivo nerve mapping to determine whether small fibers, below the resolution of IVCM, are affected. In addition to the SBNP, deep, large stromal nerves are also visible on confocal examination. However, due to large differences in nerve fiber depth and orientation, the utility of stromal nerve evaluation as a repeatable diagnostic marker is limited.[75]

Most morphometric studies have used manual tracing of the SBNP, using either an off-line software program with a tracing tool or an electronic pad and grip pen. Once traced, image analysis programs can be used to calculate morphological metrics, such as nerve fiber length, density, and branching. Examples of semi-automated programs include NeuronJ, a

semi-automated plug-in module for ImageJ, and the CCMetrics system, a custom software program developed at the University of Manchester.[76,77]

More recently, automated software programs have been developed with the goal of establishing objective, standardized methodology for morphological assessment of the SBNP.[24,77–80] Automation of corneal nerve fiber tracing has the advantage of significantly reducing the time associated with manual analysis. It also helps to standardize data collection in large, longitudinal studies where multiple observers may be required. Such standardization of IVCM for measuring the SBNP is necessary to facilitate the global implementation of this technique for clinical, diagnostic use. While automated techniques show good agreement with manual and semi-automated programs, manual methods tend to report higher numbers for nerve fiber length.[77] Reasons for this include the detection of more low contrast nerves, which may be missed by automation. Other common artifacts that may be introduced by automation include the misidentification of dendritic cells and fibrotic tissue, which may be mislabeled as nerve branches. To date, automated programs are all custom designed in house and are not commercially available; thus, validation of any of these programs by multiple laboratories is lacking.[79–84]

Over the past decade, IVCM has been widely used to study changes in the SBNP in dry eye, keratoconus, corneal infection, during contact lens wear, and in response to systemic disease and therapy.[75,85–87] As detailed below, in patients with diabetes, quantitative assessment of subbasal nerve morphology assessed by IVCM has been shown to be highly sensitive in detecting early stages of peripheral neuropathy, compared to more invasive techniques such skin punch biopsies.[87–90]

A. Morphometric Parameters

As detailed below, changes in the pattern of corneal innervation can be assessed using quantitative outcome measures, such as nerve length, density, tortuosity, and inferior whorl length. With these techniques, significant differences have been identified between normal and diabetic subjects, which may precede the development of diabetic retinopathy (Figure 8). Other, less commonly used morphometric parameters not covered here include beading,[91] branching, reflectivity,[75,86,92–94] and fiber diameter.[75,82,86]

1. Nerve Fiber Length—Nerve fiber length has been proposed as one of the most sensitive, reliable indicators for early neuropathic damage in the cornea, particularly since it does not appear to be altered during the course of normal aging or contact lens wear, and has been shown to be fairly constant over time.[95–98] It is calculated by measuring the total length of all visible nerve fibers within an image per area and is expressed as mm/mm^2. There is a large degree of variability in values reported among different research groups (range from 3.9 to 27.5 mm/mm^2).[84,87,90,99–101] Even within the same research group, nerve fiber length across subjects has been shown to vary by as much as 25.3 mm/mm^2, with a reported variance range of 9.9 mm/mm^2 to 35.2 mm/mm^2.[102] This large variance can be problematic for applying this parameter as a global diagnostic criterion, as a normal value by one group may reflect a reduced or pathological value in another.[102] Some of the variables that can affect nerve fiber length determination include the type of microscope that was used

to scan the cornea, the quality of the images selected for analysis, the analytical method used, and the adequacy of control for regional variations in the SBNP during scanning.

2. Nerve Fiber Density—Nerve fiber density is most commonly reported as the number of fibers per mm^2, although some reports have defined nerve density as the number of nerve fibers within an image or combined length of all nerve fibers within a single scan.[103–105] After manual or semi-automatic tracing, most external software programs can be used to quantitate nerve fiber density, such as NeuronJ.[76]

Nerve fiber density has been widely studied in multiple corneal and systemic diseases.[91] In diabetes, nerve fiber density is negatively correlated with HbA1c levels.[99] Thus, attaining better disease control can result in a measurable increase in nerve fiber density. This is in contrast to nerve fiber length, which is not impacted by an improvement in disease management. A range of nerve fiber densities have been reported with different confocal microscope systems.[34] This finding is likely due to differences in image resolution, contrast, and brightness as opposed to biological effects.[34] The effect of age on the density of the SBNP is controversial.[81]

There is a loss in nerve fibers under the flap following LASIK, and early signs of regeneration using IVCM are evident about one month postoperatively.[106] In addition to reduced density, some of these fibers are abnormally curved in appearance, of small diameter, and are non-branching. Reduced density is likewise seen following penetrating keratoplasty even years after the procedure, and variable results on density have been reported in both Sjögren syndrome and non-Sjögren syndrome dry eye.[24,106] Similar to nerve fiber length, measurements of normal nerve fiber density can vary widely across the cornea, with ranges from 62.5 fibers/mm^2 to 706.3 fibers/mm^2.[102]

3. Tortuosity—In animal models, a marked increase in nerve fiber tortuosity occurs as a consequence of nerve regeneration.[107] In human studies, an increase in tortuosity of the SBNP has been reported in subjects with keratoconus, Sjögren syndrome, pseudoexfoliation syndrome, rheumatoid arthritis, and following penetrating keratoplasty. Tortuosity is also associated with the severity of diabetic peripheral neuropathy. Initial reports measuring tortuosity of the SBNP used a subjective grading scale.[92] Tortuosity was classified using a 5-point scale ranging from 0 to 4, with 0 being a straight nerve fiber and 4 being considered highly tortuous. However, this produced a high degree of variability in tortuosity scores and a low level of reproducibility among different laboratories. In efforts to standardize this process, Kallinikos proposed the first objective measurement scale that was modeled after measurement scales used for assessing vascular tortuosity.[108] Nerve fibers were manually traced off-line and the tortuosity coefficient (**TC**) was determined using a custom MatLab program. Calculation of the TC took into account only the main nerve fibers and did not include smaller nerve branches in the analysis. One of the problems with using a standardized approach such as this is that nerve fiber numbers varied between scans, and different proportions of nerve fibers in each image exhibited a large amount of variance in their degree of tortuosity. Thus, automated measures of the TC did not necessarily correlate with clinical assessment.

To address this issue, Edwards et al calculated nerve fiber tortuosity measurements by correcting for the length of the nerve fiber.[100] They used custom-designed software (CCMetrics) that allowed for semi-automated analysis of nerve fiber tortuosity and total nerve fiber length. To determine tortuosity, the software assigned an arbitrary unit from 0 to 1. A value of 0 using this model indicated minimal-to-no tortuosity. Tortuosity increased as the value approached 1. The tortuosity-standardized nerve fiber length was then determined by dividing the total nerve fiber length by the unit measure of tortuosity. Using the corrected TC, they were able to better detect changes in the SBNP in diabetics compared to healthy controls, regardless of neuropathy status. They concluded that the corrected value of the TC had a greater predictive value than measures of corneal nerve fiber length for assessing neuropathic damage in diabetes.

A fully automated program for calculating tortuosity of the SBNP that incorporates an algorithm for automatic tracing of nerve fibers has since been reported. The method, reported by Scarpa and colleagues, can be readily applied to nerve fibers of different length.[109] Using a segmented approach, they calculated the ratio of the total number of twists (or changes in the sign of curvature) in the nerve fiber to the length of each nerve fiber segment. By accounting for the local contributions of highly tortuous segments in the final tortuosity score, the index allows for a standardized grade of global nerve tortuosity that is in good agreement with a qualitative clinical assessment by a trained practitioner. This index also showed a strong correlation between changes in corneal sensitivity, as measured by the Cochet-Bonnet aesthesiometer, and tortuosity score.

Annunziate also reported a novel algorithm for automatic quantification of corneal nerve tortuosity using a multiple scale, supervised learning approach.[110] This is a highly sophisticated method that uses custom algorithms to automatically select and discriminate specific shape features of the nerve fiber, including the number of inflection points and curvature. To validate their results, images were manually assessed using a four category scale (normal, mild, high, and severe) by a panel of three ophthalmologists and compared to the computed values. Overall, there was generally good agreement between clinical scoring and values obtained using automation, ranging from 76%–88%.

4. Inferior Whorl Length—In animal studies where the cornea was imaged ex vivo, changes in the inferior whorl-like pattern have been reported in diabetes.[45,111] Davidson et al reported that changes in the whorl-like vortex occurred prior to damage in other regions of the SBNP.[111] One potential mechanism accounting for this observation is that the distal ends of the nerves located within the vortex are affected before the proximal regions. This would be consistent with loss of neural function in long afferents running from the foot in peripheral neuropathic disease and may represent an early marker for patients with neuropathy.

Only one paper has evaluated measurable changes in the inferior whorl in diabetic subjects.[101] Using the section mode in the HRT software (which collects an image each time the foot pedal is pressed), they scanned the central and inferior cornea. To image the central cornea, the subjects' viewing direction was controlled by having the subject focus on the attached fixation light. The target was then moved to direct their gaze upward, until the

inferior vortex was centered within the image. Images were then collected from the central cornea, the inferior vortex, and immediately adjacent areas. For analysis, images were manually selected and traced. A custom software program was used to calculate the total length of all nerve fibers within the vortex in mm/mm^2. In normal subjects, there was a mean inferior whorl length of 31.5 mm/mm^2, which was slightly lower than previously reported.[112] This value was significantly reduced in diabetic subjects and was moderately correlated with both length and density of the nerve fibers. In their study of the dynamics of SBNP movement over time, Patel and colleagues reported that the SBNP is not static and undergoes a pattern of centripetal migration.[77] Further studies are required to investigate the influence of migratory changes on the repeatability of inferior whorl length as a surrogate marker for peripheral neuropathy.

B. Wide-field Reconstruction and Mapping of the Subbasal Nerve Plexus

Nerve fibers within the SBNP converge in a radial-like pattern toward the corneal apex. Approximately 1–2 mm below the apex, this radial arrangement typically results in a clockwise whorl-like spiral pattern. One limitation of corneal confocal imaging of the SBNP is that it has a limited field of view. Recent studies have demonstrated that collecting several single (non-overlapping) confocal images is sufficient for detecting differences in morphological parameters between healthy and diseased states. Specifically, Vagenas and Efron reported on results from 20 patients, all with Type 2 diabetes mellitus and varying levels of neuropathy.[113] They acquired 20 images throughout the central 2.5 mm^2 of the cornea, and morphological parameters of nerve fiber length and nerve branch density were calculated. Based upon their findings, they estimated that eight images of the central cornea, each with less than 20% overlap, are sufficient to adequately sample nerve branch density, and 5 images are sufficient for assessment of nerve fiber length. Nonetheless, in order to map temporal changes in the overall organization and nerve branching patterns over large areas of the cornea, the generation of image montages to expand the field of view is required.

Several groups have employed a mix of wide-field mapping techniques to enable the generation of a more complete picture of the SBNP architecture. These techniques have been applied to investigate SBNP changes in keratoconus, orthokeratology, and diabetes. While the resulting mosaic images are elegant and informative, they require hundreds of images, and manual off-line generation of these large-scale montages can require 10–20 hours per cornea. Patel and McGee reported the first wide-field images of the SBNP within the central 5–6 mm of the cornea in 2005 (Figure 9).[114] To control the viewing direction during scanning to ensure no missing gaps in the final mosaic, they used a fixation grid with 17 spot targets, each separated by 6 cm horizontally and 7 cm vertically. The grid was placed 1.1 m from the patients. Scanning time took 50 minutes to complete per patient and resulted in the manual acquisition of over 700 images, which were then manually mapped to form the final mosaic. Using this same technique, in 2008, they again mapped out the central 5–6 mm of the corneal SBNP.[74] By performing repeat scans over a period of 6 weeks, they were able to track key features such as branch points and the inferior whorl pattern, and show that the SBNP is a highly dynamic structure, moving upwards of 26 μm per week.

The second group to use mosaic imaging to construct the SBNP was Yokogawa and colleagues.[115] They used manual scanning and off-line processing to evaluate the pattern and location of Kobayashi (**K**) structures in relation to the anterior corneal mosaic, which are formed in response to compression by the planar applanating tip of the microscope. K-structures range in width from 5–15 μm, are present in the anterior stroma just underneath Bowman's layer, and have been hypothesized to represent the transverse sutural lamellae that insert into Bowman's layer in the human cornea. In contrast to the work by Patel and McGee, Yokogawa et al did not use a defined fixation target, which resulted in patchy, subconfluent montage generation.

Lum was the first to use wide-field mapping of the SBNP to evaluate qualitative changes following orthokeratology contact lens wear.[116] While in sequence scan mode, they used a moving white light as a fixation target, which moved in a linear pattern that was 11 cm × 13 cm in size. The LCD screen was placed 70 cm from the patient's eye and the patient was asked to track the white light, with optimal visual correction in place. This resulted in a scanned area of 2.5 mm horizontally × 3 mm vertically and took about 10 minutes to complete. Montage images containing 400–700 scans were generated using Photoshop. Following IVCM, corneal topography was performed on the same eye. Using this methodology, the authors described a loss of the inferior whorl pattern and an increase in tortuosity during contact lens wear that corresponded to lens-induced topographical changes. They further reported that the fibrillary lines seen by clinical biomicroscopic examination corresponded to the thickest of the redirected nerve bundles. Interestingly, the global re-distribution of nerve fibers in orthokeratology lens wear was similar to that reported in keratoconus.[117]

More recent studies have implemented a fixation target consisting of 13 radial loops that all start from a single origination point, using the inferior whorl as a key-positioning landmark.[118] A single sequence scan, taking approximately 20 seconds, was acquired for each loop. The fixation target for this study was placed 1.5 m from the front of the cornea and consisted of a moving target on a computer screen. While patient scanning time was reduced by half compared to the work by Patel and McGee, it has been argued that this method lacks sufficient detail to reliably quantitate nerve changes,[119] due to the presence of tissue artifacts generated by applanation and the absence image processing to control for motion-induced artifacts.

Misra et al also used the spot fixation grid presented by Patel and McGee to manually generate montages from both eyes of 6 subjects.[112] Scans were acquired using section mode with the grid positioned at 1 m. This allowed for a scanning area of 4 mm × 4 mm. Using this method, they compared differences in the SBNP between the right and left eyes. Interestingly, unlike corneal topography that shows "mirror image" symmetry in shape between corneas, they were unable to detect this same difference in the SBNP using this method. This study highlights the importance of wide-field mapping of the SBNP to detect global differences in the architecture of the SBNP, as these observations would not be discernable by single scan analysis.

Turuwhenua reported on the development of novel software that used feature-based image stitching of prerecorded image sequences for automated montage generation.[120] In this process, automated image rejection was used to remove images that did not contain enough detail or had tissue artifacts, such as presence of corneal epithelium or basement membrane. Images are then grouped into small clusters and compared for similarity. The inclusion of an image clustering step allowed for a decrease in the number of images that require alignment. Once stitched, the montage undergoes post-imaging processing to produce a final blended image. With this method, montages from a single cornea can be created in under 3 hours.

In the most recent report, Allgeier used a continuously moving outward spiraling fixation target placed in front of the non-scanned eye.[121] The fixation target consisted of a small display screen (640 × 480 pixels) with a black circular dot on a white background. The black dot was 5 pixels in diameter. Affixed to the screen was an eyecup that was used to eliminate outside visual stimuli. Using this technique, a montage with an area of up to 18 mm^2 was generated. For each examination, both speed (pixels/sec) and the spiral winding gap (pixels) were held constant. Four separate examinations were performed on each of 12 subjects, with speed and spiral winding gap varied in each run. While faster speeds allowed for larger areas to be scanned, slower speeds allowed for better manual adjustment to maintain focus on the SBNP. Direct streaming software was used to acquire continuous sequence scans over several minutes. Images were then registered and assembled into a montage by weighted averaging. This resulted in the generation of a composite image from 2541 single image frames (Figure 10). Post-image processing time was minimal, taking an average of 30 minutes. One difficulty with this technique is that scanning needs to begin at the corneal apex, as scans become oblique with eye movement. This can result in imaging out of the SBNP focal plane, which limits the overall area of the cornea that can be scanned. Future incorporation of an automated depth focus control may further enhance this technique.

To demonstrate the benefit of wide-field sampling, Winter et al recently reported on a software-based automated wide-field reconstruction that allowed for calculation of nerve parameters in the total region and compared them to individually sampled areas of similar size.[102] This permitted a large field of view while controlling for compression artifacts and illumination fall-off, which is frequently observed in individual scans. Total reconstruction time using this method was long, on the order of 15 hours, while image registration, segmentation, and analysis was around 30 minutes. Their data showed that the use of single scans within a limited field of view is highly subject to examiner bias, and that averaging of multiple minimally overlapping scans does not necessarily reflect an accurate determination of nerve fiber values, as previously suggested.[113]

One group has reported using the automated real time (**ART**) composite mode of the HRT-RCM.[122] ART allows for continuous online generation of large maps of the SBNP at the time of scanning. This is accomplished by manual adjustment of the scanning head position or in combination with careful control of eye movements through fixation by the contralateral eye. In this study, viewing direction was controlled by use of the attached red fixation light. This resulted in generation of a map of the SBNP up to 3.2 mm × 3.2 mm in size. The advantages of this method are that scanning time is relatively short, taking only 3 minutes or less to collect the images, and no post-image processing is required. In addition,

since images are acquired in real time, quality control occurs simultaneously, resulting in optimal image acquisition. A potential drawback to this technique, however, is the level of expertise required by the examiner, with increasing skill required for larger montages.

C. 3-D Reconstruction of the Subbasal Nerve Plexus

It has been suggested that compression artifacts in 2-D images along with microsaccadic eye movements may affect accurate assessment of nerve fiber length. To address this issue, Allgeier et al used a phase correlation algorithm to control for motion distortion.[38] In their dataset, images were acquired in the z-scan volume mode with a 4-second acquisition time. Following this, images were registered using a custom program in C++ and volumetrically reconstructed by serially stacking up each registered scan (Figure 11). The nerve fiber layer was then extracted from the 3-D volume stack by first manually placing a seed point within the nerve fiber layer, then tracing along the brightest pixels in the image. These tracings were used to generate a depth map that can be visualized using an Interactive 3-D Surface plot plug-in (ImageJ, NIH). It took only about 3 minutes to register and extract data from the 3-D volume sets.

Zhihov et al also measured length of the SBNP using images acquired in the z-scan volume mode of the HRT-RCM.[84] Imaging time was longer, taking approximately 15 minutes. They did not correct for motion or compression artifacts. Instead, they used a custom algorithm for automatic segmentation of the nerve fibers, followed by skeletonization. Images were skeletonized using a one pixel-wide line segment, and morphological parameters were assessed before and after skeletonization. A custom algorithm reported by Dehghani et al incorporated a linear 2D Gabor filter tuned to the orientation of the nerve fiber with a Gaussian envelope. This design allowed for enhancement of the foreground features while reducing background noise.[79] This same group has since extended this latter method to include multiples scales and pixel classification. While they found this method to be superior to their single scale model, significant expertise is required by the examiner to complete the analysis.[80]

Ziegler et al developed a novel algorithm that mapped nerve fibers from montaged 3-D volume stacks.[82] A modified volume scan was performed on each patient by continuously oscillating the focal plane back and forth to cover the full height of the anterior corneal mosaic ridges. Scan time using this method was about 15 minutes per patient. Images were corrected for motion-induced artifacts, and volume stacks containing 96–120 images were reconstructed to allow for the development of a depth map of the SBNP. Images were then montaged and nerves were segmented and thinned to a thickness of 1 pixel. The resultant thinned fiber network was used for automatic analysis of nerve parameters. Using this technique, the authors concluded that nerve fiber density, and not nerve fiber length, was more predictive for neuropathy in diabetes.

IV. Conclusions

Confocal microscopy has the ability to noninvasively resolve structural and functional interrelationships, both temporally and spatially, in the corneas of research animals and human patients in vivo. With use of confocal microscopy, the cellular details of fundamental

biological processes, such as inflammation, wound healing, toxicity, infection, and disease, which could previously be studied only under static or isolated conditions, can be dynamically evaluated over time and the effectiveness of treatment modalities determined. The development and application of new hardware and software for 3-D scanning, wide-field mapping and morphometric analysis with the HRT-RCM continues to expand the potential applications of this unique imaging technology for quantitative in vivo corneal imaging.

Acknowledgments

This study was supported in part by NIH R01 EY013322, EY024433, EY024546, NIH P30 EY020799, OneSight Research Foundation (DMR), and an unrestricted grant from Research to Prevent Blindness, Inc., NY, NY.

REFERENCES

1. Kobayashi A, Mawatari Y, Yokogawa H, Sugiyama K. In vivo laser confocal microscopy after Descemet stripping with automated endothelial keratoplasty. Am J Ophthalmol. 2008; 145:977–985. [PubMed: 18400202]
2. Bouheraoua N, Jouve L, El Sanharawi M, et al. Optical coherence tomography and confocal microscopy following three different protocols of corneal collagen-crosslinking in keratoconus. Invest Ophthalmol Vis Sci. 2014; 55:7601–7609. [PubMed: 25352122]
3. Petroll WM, Jester JV, Cavanagh HD. Clinical confocal microscopy. Curr Opin Ophthalmol. 1998; 9:59–65. [PubMed: 10387471]
4. Tervo T, Moilanen J. In vivo confocal microscopy for evaluation of wound healing following corneal refractive surgery. Prog Retin Eye Res. 2003; 22:339–358. [PubMed: 12852490]
5. Kaufman SC, Kaufman HE. How has confocal microscopy helped us in refractive surgery? Curr Opin Ophthalmol. 2006; 17:380–388. [PubMed: 16900032]
6. Petroll, WM.; Cavanagh, HD.; Jester, JV. Confocal microscopy. In: Krachmer, J.; Mannis, M.; Holland, E., editors. Cornea. St. Louis: Elsevier; 2011. p. 205-220.
7. Jester JV, Petroll WM, Cavanagh HD. Corneal stromal wound healing in refractive surgery: the role of the myofibroblast. Prog Retinal Eye Res. 1999; 18:311–356.
8. Labbe A, Khammari C, Dupas B, et al. Contribution of in vivo confocal microscopy to the diagnosis and management of infectious keratitis. Ocul Surf. 2009; 7:41–52. [PubMed: 19214351]
9. Efron N, Morgan PB, Makrynioti D. Chronic morbidity of corneal infiltrative events associated with contact lens wear. Cornea. 2007; 26:793–799. [PubMed: 17667611]
10. Vaddavalli PK, Garg P, Sharma S, Sangwan VS, et al. Role of confocal microscopy in the diagnosis of fungal and acanthamoeba keratitis. Ophthalmology. 2011; 118:29–35. [PubMed: 20801515]
11. Imayasu M, Petroll WM, Jester JV, et al. The relationship between contact lens oxygen transmissibility and binding of pseudomonas aeruginosa to the cornea after overnight wear. Ophthalmology. 1994; 101:371–386. [PubMed: 8115159]
12. Ren DH, Yamamoto K, Ladage PM, et al. Adaptive effects of 30-night wear of hyper-O2 transmissible contact lenses on bacterial binding and corneal epithelium: A 1 year clinical trial. Ophthalmology. 2002; 109:27–39. [PubMed: 11772575]
13. Cavanagh HD, Ladage PM, Li SL, et al. Effects of daily and overnight wear of a novel hyper oxygen-transmissible soft contact lens on bacterial binding and corneal epithelium: a 13-month clinical trial. Ophthalmology. 2002; 109:1957–1969. [PubMed: 12414399]
14. Ladage PM, Yamamoto K, Ren DH, et al. Effects of rigid and soft contact lens daily wear on corneal epithelium, tear lactate dehydrogenase, and bacterial binding to exfoliated epithelial cells. Ophthalmology. 2001; 108:1279–1288. [PubMed: 11425688]
15. Robertson DM, Petroll WM, Cavanagh HD. The effect of nonpreserved care solutions on 12 months of daily and extended silicone hydrogel contact lens wear. Ophthalmology. 2008; 49:7–15.

16. Erie JC, Patel SV, McLaren JW, et al. Corneal keratocyte deficits after photorefractive keratectomy and laser in situ keratomileusis. Am J Ophthalmol. 2006; 141:799–809. [PubMed: 16545332]
17. Patel SV, McLaren JW, Hodge DO, Bourne WM. Normal human keratocyte density and corneal thickness measurement by using confocal microscopy in vivo. Invest Ophthalmol Vis Sci. 2001; 42:333–339. [PubMed: 11157863]
18. Erie JC, Nau CB, McLaren JW, et al. Long-term keratocyte deficits in the corneal stroma after LASIK. Ophthalmology. 2004; 111:1356–1361. [PubMed: 15234137]
19. Ku JY, Niederer RL, Patel DV, et al. Laser scanning in vivo confocal analysis of keratocyte density in keratoconus. Ophthalmology. 2008; 115:845–850. [PubMed: 17825419]
20. Niederer RL, Perumal D, Sherwin T, McGhee CN. Laser scanning in vivo confocal microscopy reveals reduced innervation and reduction in cell density in all layers of the keratoconic cornea. Invest Ophthalmol Vis Sci. 2008; 49:2964–2970. [PubMed: 18579760]
21. Efron N. Contact lens-induced changes in the anterior eye as observed in vivo with the confocal microscope. Prog Retin Eye Res. 2007; 26:398–436. [PubMed: 17498998]
22. Zhivov A, Guthoff RF, Stachs O. In vivo confocal microscopy of the ocular surface: from bench to bedside and back again. Br J Ophthalmol. 2010; 94:1557–1558. [PubMed: 20805140]
23. Dhaliwal JS, Kaufman SC, Chiou AGY. Current applications of clinical confocal microscopy. Curr Opin Ophthalmol. 2007; 18:300–307. [PubMed: 17568206]
24. Villani E, Baudouin C, Efron N, et al. In vivo confocal microscopy of the ocular surface: from bench to bedside. Curr Eye Res. 2014; 39:213–231. [PubMed: 24215436]
25. Zhivov A, Stachs O, Kraak R, et al. In vivo confocal microscopy of the ocular surface. Ocul Surf. 2006; 4:81–93. [PubMed: 16681079]
26. Erie JC, McLaren JW, Patel SV. Confocal microscopy in ophthalmology. Am J Ophthalmol. 2009; 148:639–646. [PubMed: 19674730]
27. Patel DV, McGhee CN. Quantitative analysis of in vivo confocal microscopy images: a review. Surv Ophthalmol. 2013; 58:466–475. [PubMed: 23453401]
28. Lemp MA, Dilly PN, Boyde A. Tandem scanning (confocal) microscopy of the full thickness cornea. Cornea. 1986; 4:205–209. [PubMed: 3836030]
29. Cavanagh HD, Shields W, Jester JV, et al. Confocal microscopy of the living eye. CLAO J. 1990; 16:65–73. [PubMed: 2407380]
30. Petroll WM, Cavanagh HD, Jester JV. Three-dimensional reconstruction of corneal cells using in vivo confocal microscopy. J Microsc. 1993; 170:213–219. [PubMed: 8371258]
31. Masters BR, Thaer AA. Real-time scanning slit confocal microscopy of the in vivo human cornea. Appl Optics. 1994; 33:695–701.
32. Brakenhoff GJ, Visscher K. Confocal imaging with bilateral scanning and array detectors. J Microsc. 1992; 165:139–146.
33. Guthoff, RF.; Baudouin, C.; Stave, J. Atlas of Confocal Laser Scanning In Vivo Microscopy in Ophthalmology. Berlin: Heidelberg/Springer; 2006.
34. Erie EA, McLaren JW, Kittleson KM, et al. Corneal subbasal nerve density: A comparison of two confocal microscopes. Eye Contact Lens. 2008; 34:322–325. [PubMed: 18997541]
35. Zhivov A, Stachs O, Stave J, Guthoff RF. In vivo three-dimensional confocal laser scanning microscopy of corneal surface and epithelium. Br J Ophthalmol. 2009; 93:667–672. [PubMed: 18650213]
36. Jester JV, Moller-Pedersen T, Huang J, et al. The cellular basis of corneal transparency: evidence for 'corneal crystallins'. J Cell Sci. 1999; 112:613–612. [PubMed: 9973596]
37. Stachs O, Zhivov A, Kraak R, et al. In vivo three-dimensional confocal laser scanning microscopy of the epithelial nerve structure in the human cornea. Graefes Arch Clin Exp Ophthalmol. 2007; 245:569–575. [PubMed: 16941142]
38. Allgeier S, Zhivov A, Eberle F, et al. Image reconstruction of the subbasal nerve plexus with in vivo confocal microscopy. Invest Ophthalmol Vis Sci. 2011; 52:5022–5028. [PubMed: 21447691]

39. Petroll WM, Cavanagh HD. Remote-controlled scanning and automated confocal microscopy through focusing using a modified HRT Rostock cornea module. Eye Contact Lens. 2009; 35:302–308. [PubMed: 19901584]
40. Li HF, Petroll WM, Moller-Pederson T, et al. Epithelial and corneal thickness measurements by in vivo confocal microscopy through focusing (CMTF). Curr Eye Res. 1997; 16:214–221. [PubMed: 9088737]
41. Li J, Jester JV, Cavanagh HD, et al. On-line 3-dimensional confocal imaging in vivo. Invest Ophthalmol Vis Sci. 2000; 41:2945–2953. [PubMed: 10967049]
42. Wiegand W, Thaer AA, Kroll P, et al. Optical sectioning of the cornea with a new confocal in vivo slit-scanning video-microscope. Ophthalmology. 1993; 100(9A):128. [PubMed: 8433817]
43. Petroll WM, Weaver M, Vaidya S, et al. Quantitative 3-D corneal imaging in vivo using a modified HRT-RCM confocal microscope. Cornea. 2013; 36:e36–e43. [PubMed: 23051907]
44. Reichard M, Hovakimyan M, Wree A, et al. Comparative in vivo confocal microscopical study of the cornea anatomy of different laboratory animals. Curr Eye Res. 2010; 35:1072–1080. [PubMed: 20961216]
45. Cai D, Zhu M, Petroll WM, et al. The impact of type 1 diabetes mellitus on corneal epithelial nerve morphology and the corneal epithelium. Am J Pathol. 2014; 184:2662–2670. [PubMed: 25102563]
46. Reinstein DZ, Archer TJ, Gobbe M, et al. Epithelial thickness in the normal cornea: Three dimensional display with very high frequency ultrasound. J Refract Surg. 2008; 24:571–581. [PubMed: 18581782]
47. Francoz M, Karamoko I, Baudouin C, Labbe A. Ocular surface epithelial thickness evaluation with spectral-domain optical coherence tomography. Invest Ophthalmol Vis Sci. 2011; 52:9116–9123. [PubMed: 22025572]
48. Correa-Perez ME, Olmo N, Lopez-Miguel A, et al. Dependability of posterior-segment spectral domain optical coherence tomography for measuring central corneal thickness. Cornea. 2014; 33:1219–1224. [PubMed: 25211358]
49. Ichijima H, Petroll WM, Jester JV, et al. In vivo confocal microscopic studies of endothelial wound healing in rabbit cornea. Cornea. 1993; 12:369–378. [PubMed: 8306656]
50. Ichijima H, Petroll WM, Barry PA, et al. Actin filament organization during endothelial wound healing in the rabbit cornea. Comparison between transcorneal freeze and mechanical scrape injuries. Invest Ophthalmol Vis Sci. 1993; 34:2803–2812. [PubMed: 8344802]
51. Petroll WM, Barry-Lane PA, Cavanagh HD, Jester JV. ZO-1 organization and myofibroblast transformation of corneal endothelial cells after freeze injury in the cat. Exp Eye Res. 1997; 64:257–267. [PubMed: 9176060]
52. Boote C, Du Y, Morgan S, et al. Quantitative assessment of ultrastructure and light scatter in mouse corneal debridement wounds. Invest Ophthalmol Vis Sci. 2012; 53:2786–2795. [PubMed: 22467580]
53. Moller-Pedersen T, Cavanagh HD, Petroll WM, Jester JV. Corneal haze development after PRK is regulated by volume of stromal tissue removal. Cornea. 1998; 17:627–639. [PubMed: 9820944]
54. Moller-Pedersen T, Cavanagh HD, Petroll WM, Jester JV. Neutralizing antibody to TGFb modulates stromal fibrosis but not regression of photoablative effect following PRK. Curr Eye Res. 1998; 17:736–737. [PubMed: 9678420]
55. Moller-Pedersen T, Cavanagh HD, Petroll WM, Jester JV. Stromal wound healing explains refractive instability and haze development after photorefractive keratectomy: A 1-year confocal microscopic study. Ophthalmology. 2000; 107:1235–1245. [PubMed: 10889092]
56. Moller-Pedersen T, Li H, Petroll WM, et al. Confocal microscopic characterization of wound repair after photorefractive keratectomy using in vivo confocal microscopy. Invest Ophthalmol Vis Sci. 1998; 39:487–501. [PubMed: 9501858]
57. Moller-Pedersen T, Vogel M, Li HF, et al. Quantification of stromal thinning, epithelial thickness, and corneal haze after photorefractive keratectomy using in vivo confocal microscopy. Ophthalmology. 1997; 104:360–368. [PubMed: 9082257]
58. Petroll M, Hagenasr D, Cavanagh H, Robertson D. 3-Dimensional assessment of in vivo corneal wound healing using a modified HRT-RCM confocal microscope (abstract). Invest Ophthalmol Vis Sci. 2013; 54 ARVO abstract #3222.

59. McLaren JW, Bourne WM, Patel SV. Standardization of corneal haze measurement in confocal microscopy. Invest Ophthalmol Vis Sci. 2010; 51:5610–5616. [PubMed: 20539002]
60. McCulley JP, Petroll WM. Quantitative assessment of corneal wound healing following IntraLASIK using in vivo confocal microscopy. Trans Am Ophthalmol Soc. 2008; 106:84–92. [PubMed: 19277224]
61. Erie JC, Patel SV, McLaren JW, et al. Effect of myopic laser in situ keratomileusis on epithelial and stromal thickness. Ophthalmology. 2002; 109:1447–1452. [PubMed: 12153794]
62. Vesaluoma M, Perez-Santonja J, Petroll WM, et al. Corneal stromal changes induced by myopic LASIK. Invest Ophthalmol Vis Sci. 2000; 41:369–376. [PubMed: 10670464]
63. Jester JV, Lee YG, Li J, et al. Measurement of corneal sublayer thickness and transparency in transgenic mice with altered corneal clarity using in vivo confocal microscopy. Vision Res. 2001; 41:1283–1290. [PubMed: 11322973]
64. Jester JV, Li H, Petroll WM, et al. Area and depth of surfactant-induced corneal injury correlates with cell death. Invest Ophthalmol Vis Sci. 1998; 39:922–936. [PubMed: 9579472]
65. Jester JV, Maurer JK, Petroll WM, et al. Application of in vivo confocal microscopy to the understanding of surfactant-induced ocular irritation. Toxicol Pathol. 1996; 24:412–428. [PubMed: 8864183]
66. Maurer JK, Li HF, Petroll WM, et al. Confocal microscopic characterization of initial corneal changes of surfactant-induced eye irritation in the rabbit. Toxicol Appl Pharmacol. 1997; 143:291–300. [PubMed: 9144446]
67. McLaren JW, Bourne WM, Patel SV. Automated assessment of keratocyte density in stromal images from the Confoscan 4 confocal microscope. Invest Ophthalmol Vis Sci. 2010; 51:1918–1926. [PubMed: 19892869]
68. Petroll WM, Boettcher K, Barry PA, et al. Quantitative assessment of anteroposterior keratocyte density in the normal rabbit cornea. Cornea. 1995; 14:3–9. [PubMed: 7712733]
69. Poole CA, Brookes NH, Clover GM. Keratocyte networks visualized in the living cornea using vital dyes. J Cell Sci. 1993; 104:353–363. [PubMed: 8505365]
70. Muller LJ, Marfurt CF, Kruse F, Tervo TM. Corneal nerves: structure, contents and function. Exp Eye Res. 2003; 76:521–542. [PubMed: 12697417]
71. Guthoff RF, Wienss H, Hahnel C, Wree A. A three-dimensional study using confocal laser scanning fluorescence microscopy. Cornea. 2005; 24:608–613. [PubMed: 15968170]
72. Marfurt CF, Cox J, Deek S, Dvorscak L. Anatomy of the human corneal innervation. Exp Eye Res. 2010; 90:478–494. [PubMed: 20036654]
73. Muller LJ, Vrensen GF, Pels L, et al. Architecture of human corneal nerves. Invest Ophthalmol Vis Sci. 1997; 38:985–994. [PubMed: 9112994]
74. Patel DV, McGhee CN. In vivo laser scanning confocal microscopy confirms that the human corneal sub-basal nerve plexus is a highly dynamic structure. Invest Ophthalmol Vis Sci. 2008; 49:3409–3412. [PubMed: 18441297]
75. Hosal BM, Ornek N, Zilelioglu G, Elhan AH. Morphology of corneal nerves and corneal sensation in dry eye: a preliminary study. Eye. 2005; 19:1276–1279. [PubMed: 15550934]
76. Cottrell P, Ahmed S, James C, et al. Neuron J is a rapid and reliable open source tool for evaluating corneal nerve density in herpes simplex keratitis. Invest Ophthalmol Vis Sci. 2014; 55:7312–7320. [PubMed: 25324286]
77. Dehghani C, Pritchard N, Edwards K, et al. Fully automated, semiautomated, and manual morphometric analysis of corneal subbasal nerve plexus in individuals with and without diabetes. Cornea. 2014; 33:696–702. [PubMed: 24886994]
78. Scarpa F, Grisan E, Ruggeri A. Automatic recognition of corneal nerve structures in images from confocal microscopy. Invest Ophthalmol Vis Sci. 2008; 49:4801–4807. [PubMed: 18614801]
79. Dabbah MA, Graham J, Petropoulos I, et al. Dual-mode automatic detection of nerve-fibres in corneal confocal microscopy images. Med Image Comput Comput Assist Interv. 2010; 13:300–307. [PubMed: 20879244]
80. Dabbah MA, Graham J, Petropoulos IN, et al. Automatic analysis of diabetic peripheral neuropathy using multi-scale quantittive morphology of nerve fibres in corneal confocal microscopy imaging. Med Image Anal. 2011; 15:738–747. [PubMed: 21719344]

81. Holmes TJ, Pellegrini M, Miller C, et al. Automated software analysis of corneal micrographs for peripheral neuropathy. Invest Ophthalmol Vis Sci. 2010; 51:4480–4491. [PubMed: 20805570]
82. Ziegler D, Papanas N, Zhivov A, et al. Early detection of nerve fiber loss by corneal confocal microscopy and skin biopsy in recently diagnosed type 2 diabetes. Diabetes. 2014; 63:2454–2463. [PubMed: 24574045]
83. Zhivov A, Peschel S, Schober HC, et al. Diabetic foot syndrome and corneal subbasal nerve plexus changes in Congolese patients with Type 2 diabetes. PLoS One. 2015; 10:e0119842. [PubMed: 25811186]
84. Zhivov A, Winter K, Hovakimyan M, et al. Imaging and quantification of subbasal nerve plexus in healthy volunteers and diabetic patients with or without retinopathy. PLoS One. 2013; 8:e52157. [PubMed: 23341892]
85. Cruzat A, Pavan-Langston D, Hamrah P. In vivo confocal microscopy of corneal nerves: analysis and clinical correlation. Semin Ophthalmol. 2010; 25:171–177. [PubMed: 21090996]
86. Benitez del Castillo JM, Wasfy MAS, Fernandez C, Garcia-Sanchez J. An in vivo confocal masked study on corneal epithelium and subbasal nerves in patients with dry eye. Invest Ophthalmol Vis Sci. 2004; 45:3030–3035. [PubMed: 15326117]
87. Tavakoli M, Mitu-Pretorian M, Petropoulos IN, et al. Corneal confocal microscopy detects early nerve regeneration in diabetic neuropathy after simultaneous pancreas and kidney transplantation. Diabetes. 2013; 62:254–260. [PubMed: 23002037]
88. Efron N. The Glenn A. Fry Award Lecture 2010: Ophthalmic markers of diabetic neuropathy. Optom Vis Sci. 2011; 88:661–683. [PubMed: 21478787]
89. Rosenberg ME, Tervo TM, Immonen IJ, et al. Corneal structure and sensitivity in type 1 diabetes mellitus. Invest Ophthalmol Vis Sci. 2000; 41:2915–2921. [PubMed: 10967045]
90. Quattrini C, Tavakoli M, Jeziorska M, et al. Surrogate markers of small fiber damage in human diabetic neuropathy. Diabetes. 2007; 56:2148–2154. [PubMed: 17513704]
91. Ishibashi F, Kawasaki A, Yamanaka E, et al. Morphometric features of corneal epithelial basal cells, and their relationship with corneal nerve pathology and clinical factors in patients with type 2 diabetes. J Diabetes Invest. 2013; 4:492–501.
92. Oliveira-Soto L, Efron N. Morphology of corneal nerves using confocal microscopy. Cornea. 2001; 20:374–384. [PubMed: 11333324]
93. Martone G, Frezzotti P, Tosi GM, et al. An in vivo confocal microscopy analysis of effects of topical antiglaucoma therapy with preservative on corneal innervation and morphology. Am J Ophthalmol. 2009; 147:725–735. [PubMed: 19181302]
94. Labbe A, Alalwani H, Van Went C, et al. The relationship between subbasal nerve morphology and corneal sensation in ocular surface disease. Invest Ophthalmol Vis Sci. 2012; 53:4926–4931. [PubMed: 22695962]
95. Efron N, Edwards K, Roper N, et al. Repeatability of measuring corneal subbasal nerve fiber length in individuals with type 2 diabetes. Eye Contact Lens. 2010; 36:245–248. [PubMed: 20724854]
96. Ahmed A, Bril V, Orszag A, et al. Detection of diabetic sensorimotor polyneuropathy by corneal confocal microscopy in type 1 diabetes: a concurrent validity study. Diabetes Care. 2012; 35:821–828. [PubMed: 22323412]
97. Dehghani C, Pritchard N, Edwards K, et al. Morphometric stability of the corneal subbasal nerve plexus in healthy individuals: a 3-year longitudinal study using corneal confocal microscopy. Invest Ophthalmol Vis Sci. 2014; 55:3195–3199. [PubMed: 24764058]
98. Wu T, Ahmed A, Bril V, et al. Variables associated with corneal confocal microscopy parameters in healthy volunteers: implications for diabetic neuropathy screening. Diabet Med. 2012; 29:e297–e303. [PubMed: 22519850]
99. Tavakoli M, Kallinikos P, Iqbal A, et al. Corneal confocal microscopy detects improvement in corneal nerve morphology with an improvement in risk factors for diabetic neuropathy. Diabet Med. 2011; 28:1261–1267. [PubMed: 21699561]
100. Edwards K, Pritchard N, Vagenas D, et al. Standardizing corneal nerve fibre length for nerve tortuosity increases its association with measures of diabetic neuropathy. Diabet Med. 2014; 31:1205–1209. [PubMed: 24750318]

101. Petropoulos IN, Ferdousi M, Marshall A, et al. The inferior whorl for detecting diabetic peripheral neuropathy using corneal confocal microscopy. Invest Ophthalmol Vis Sci. 2015 Epub ahead of print:
102. Winter K, Scheibe P, Kohler B, et al. Local variability of parameters for characterization of the corneal subbasal nerve plexus. Curr Eye Res. 2015:1–13. Epub ahead of press: [PubMed: 25803579]
103. Midena E, Brugin E, Ghirlando A, et al. Corneal diabetic neuropathy: a confocal microscopy study. J Refract Surg. 2006; 22:S1047–S1052. [PubMed: 17444092]
104. Grupcheva CN, Wong T, Riley AF, McGhee CN. Assessing the sub-basal nerve plexus of the living healthy human cornea by in vivo confocal microscopy. Clin Experiment Ophthalmol. 2002; 30:187–190. [PubMed: 12010212]
105. Erie JC, McLaren JW, Hodge DO, Bourne WM. The effect of age on the corneal subbasal nerve plexus. Cornea. 2005; 24:705–709. [PubMed: 16015090]
106. Stachs O, Zhivov A, Kraak R, et al. Structural-functional correlations of corneal innervation after LASIK and penetrating keratoplasty. J Refract Surg. 2010; 26:159–167. [PubMed: 20229947]
107. Kawabuchi M, Chongjian Z, Islam AT, et al. The effect of aging on the morpological nerve changes during muscle reinnvervation after nerve crush. Restor Neurol Neurosci. 1998; 13:117–127. [PubMed: 12671273]
108. Kallinikos P, Berhanu M, O'Donnell C, et al. Corneal nerve tortuosity in diabetic patients with neuropathy. Invest Ophthalmol Vis Sci. 2004; 45:418–422. [PubMed: 14744880]
109. Scarpa F, Zheng X, Ohashi Y, Ruggeri A. Automatic evaluation of corneal nerve tortuosity in images from in vivo confocal microscopy. Invest Ophthalmol Vis Sci. 2011; 52:6404–6408. [PubMed: 21775658]
110. Annunziata, R.; Kheirkhah, A.; Aggarwal, S., et al. Tortuosity classification of corneal nerves images using a multiple-scale-multiple-window approach. In: Chen, X.; Garvin, MK.; Liu, JJ., editors. Proceedings of the Ophthalmic Medical Image Analysis First International Workshop. Boston, MA: OMIA 2014; 2014 Sep 14. p. 113-120.Iowa Research Online; 2014, available from: http://ir.uiowa.edu/omia/2014_Proceedings/2014/15/
111. Davidson EP, Coppey LJ, Kardon RH, Yorek MA. Differences and similarities in development of corneal nerve damage and peripheral neuropathy and in diet-induced obesity and type 2 diabetic rats. Invest Ophthalmol Vis Sci. 2014; 55:1222–1230. [PubMed: 24519423]
112. Misra S, Craig JP, McGhee CN, Patel DV. Interocular comparison by in vivo confocal microscopy of the 2-dimensional architecture of the normal human corneal subbasal nerve plexus. Cornea. 2012; 31:1376–1380. [PubMed: 22257862]
113. Vagenas D, Pritchard N, Edwards K, et al. Optimal image sample size for corneal nerve morphometry. Optom Vis Sci. 2012; 89:812–817. [PubMed: 22407254]
114. Patel DV, McGhee CN. Mapping of the normal human corneal sub-Basal nerve plexus by in vivo laser scanning confocal microscopy. Invest Ophthalmol Vis Sci. 2005; 46:4485–4488. [PubMed: 16303938]
115. Yokogawa H, Kobayashi A, Sugiyama K. Mapping of normal corneal K-Structures by in vivo laser confocal microscopy. Cornea. 2008; 27:879–883. [PubMed: 18724147]
116. Lum E, Golebiowski B, Swarbrick HA. Mapping the corneal sub-basal nerve plexus in orthokeratology lens wear using in vivo laser scanning confocal microscopy. Invest Ophthalmol Vis Sci. 2012; 53:1803–1809. [PubMed: 22395884]
117. Patel DV, McGhee CN. Mapping the corneal sub-basal nerve plexus in keratoconus by in vivo laser scanning confocal microscopy. Invest Ophthalmol Vis Sci. 2006; 47:1348–1351. [PubMed: 16565367]
118. Edwards K, Pritchard N, Gosschalk K, et al. Wide-field assessment of the human corneal subbasal nerve plexus in diabetic neuropathy using a novel mapping technique. Cornea. 2012; 31:1078–1082. [PubMed: 23045727]
119. Patel DV, McGhee CNJ. Techniques for wide-field assessment of the human corneal subbasal nerve plexus: letter to the editor. Cornea. 2013; 32:e140–e141. [PubMed: 23572133]

120. Turuwhenua JT, Patel DV, McGhee CN. Fully automated montaging of laser scanning in vivo confocal microscopy images of the human corneal subbasal nerve plexus. Invest Ophthalmol Vis Sci. 2012; 53:2235–2242. [PubMed: 22427563]

121. Allgeier S, Maier S, Mikut R, et al. Mosaicking the subbasal nerve plexus by guided eye movements. Invest Ophthalmol Vis Sci. 2014; 55:6082–6089. [PubMed: 25159207]

122. Zhivov A, Blum M, Guthoff R, Stachs O. Real-time mapping of the subepithelial nerve plexus by in vivo confocal laser scanning microscopy. Br J Ophthalmol. 2010; 94:1133–1135. [PubMed: 20813752]

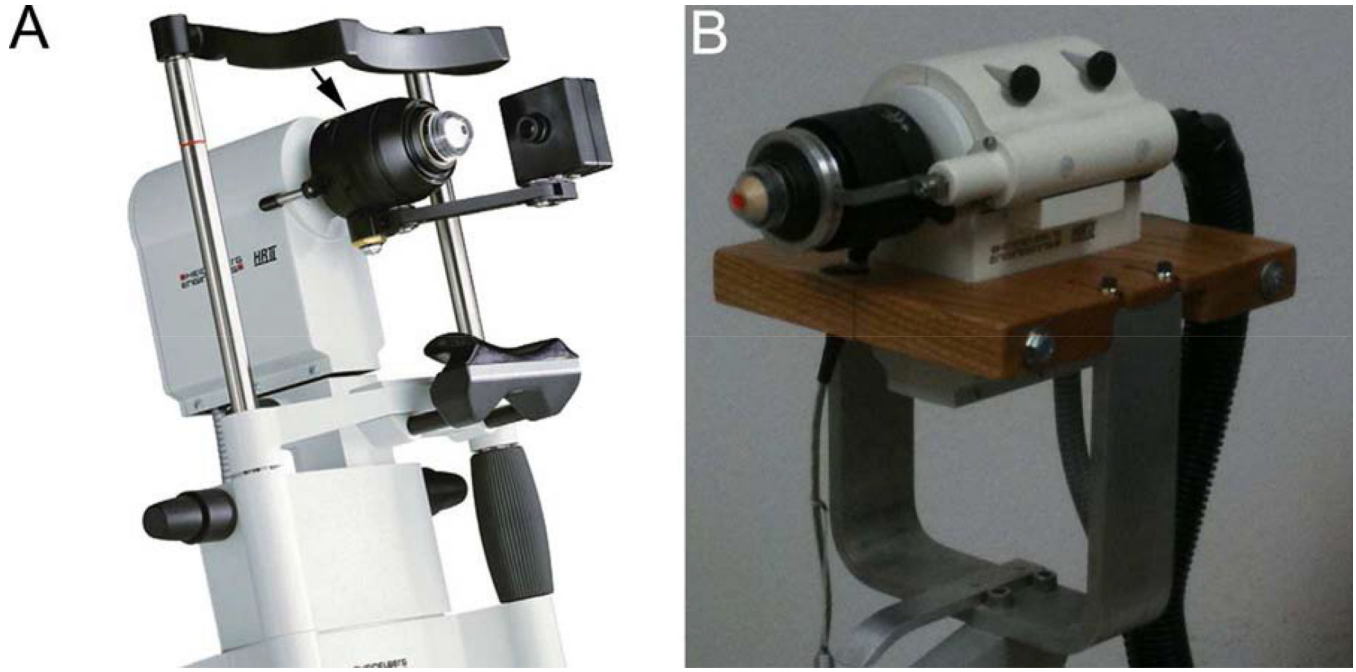

Figure 1.

A. Heidelberg Engineering HRT-RCM confocal microscope (From Heidelberg Engineering Website). Arrow denotes thumbscrew drive which is turned by hand to change position of focal plane. B. Modified HRT-RCM with motor drive to allow automated through focusing, and modified support structure (slit lamp stand) to facilitate positioning. (Reprinted with permission from Petroll WM, Weaver M, Vaidya S, et al.Quantitative 3-dimensional corneal imaging in vivo using a modified HRT-RCM confocal microscope. *Cornea* 2013;32:e36–43.)

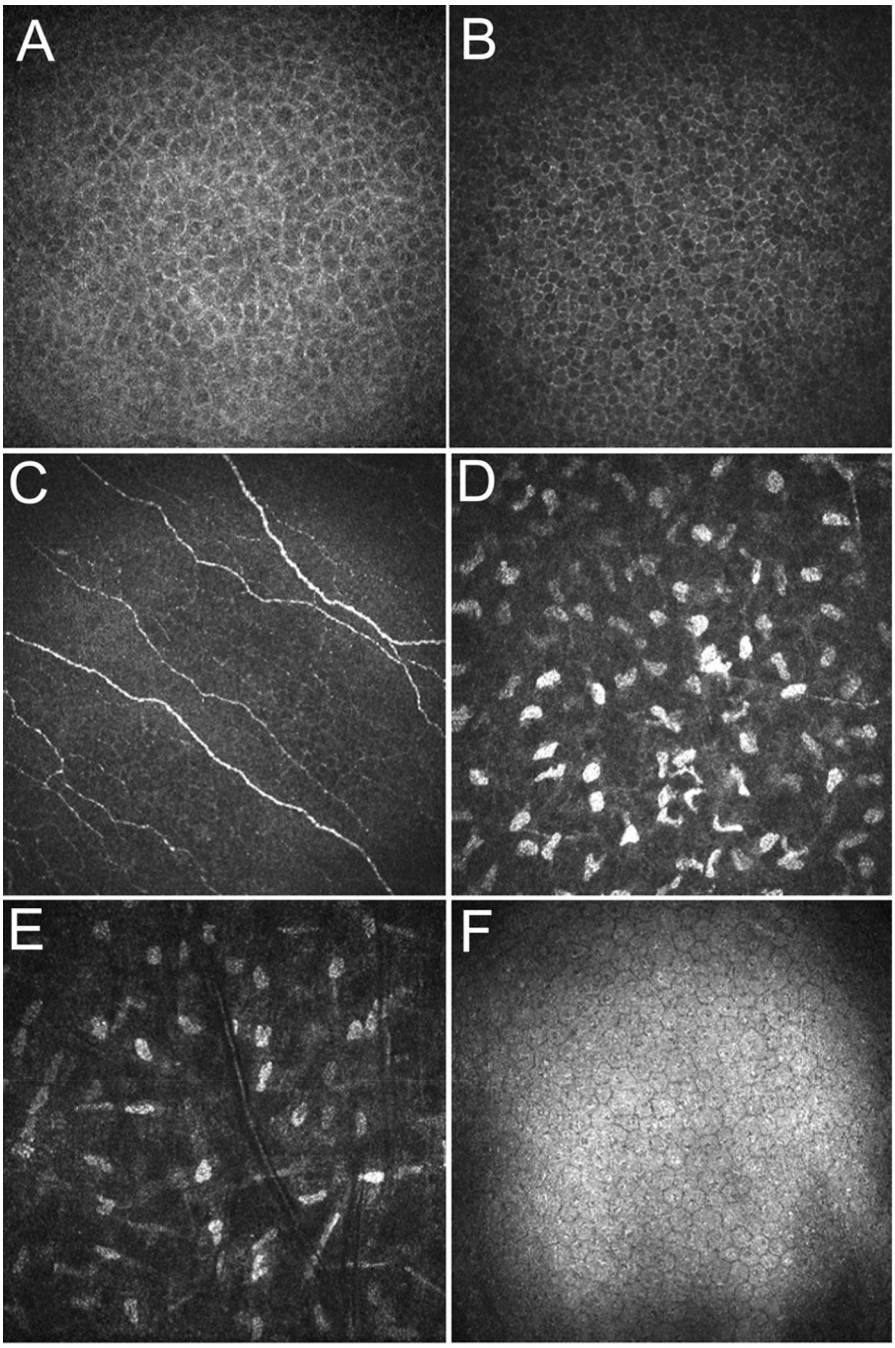

Figure 2.

Images of a normal human cornea obtained using the HRT-RCM. **A**. Epithelial wing cells. **B**. Basal epithelial cells. **C**. Epithelial nerve plexus. **D**. Anterior stroma just below Bowman's layer. **E**. Midstroma. Note decreased density of keratocyte nuclei as compared to **D**. **F**. Normal endothelium. Horizontal field width = 400 μm. (Reprinted with permission from Petroll WM, Cavanagh HD, Jester JV. Confocal microscopy, in Krachmer J, Mannis M, Holland (eds). *Cornea.* (St Louis, Elsevier, 2010, pp 205-20.)

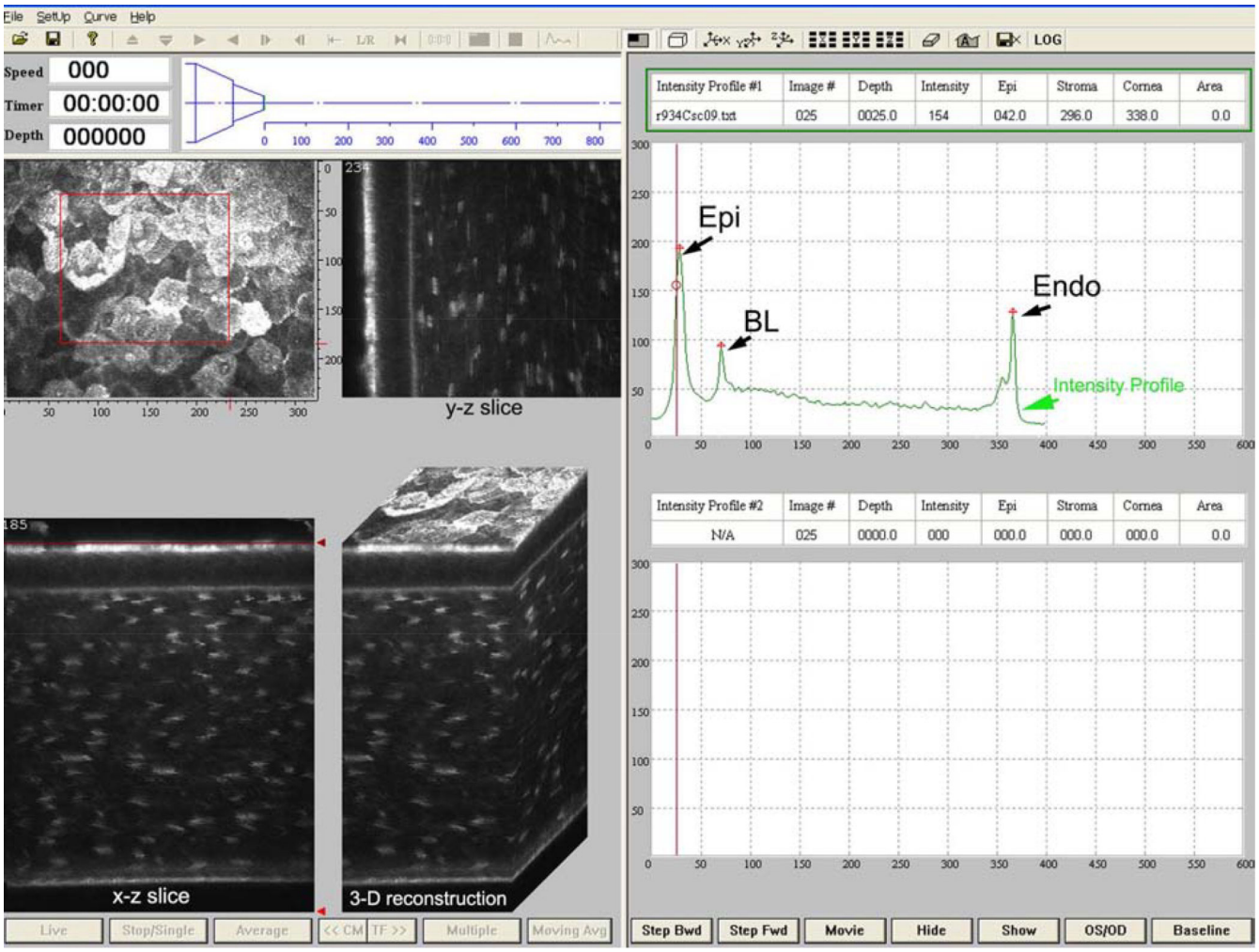

Figure 3.

Screen shot of HRT-RCM CMTF program. Scan shown is from a rabbit cornea. Right side shows corneal intensity curve with intensity peaks at the superficial epithelium (Epi), basal lamina (BL), and endothelium (Endo). Images on the left are reconstructions of the image stack collected by CMTF imaging shown at different projection angles. Scan shown was collected at a speed of 30 μm/second. (Reprinted with permission from Petroll WM, Weaver M, Vaidya S, et al. Quantitative 3-dimensional corneal imaging in vivo using a modified HRT-RCM confocal microscope. *Cornea* 2013;32:e36–43.)

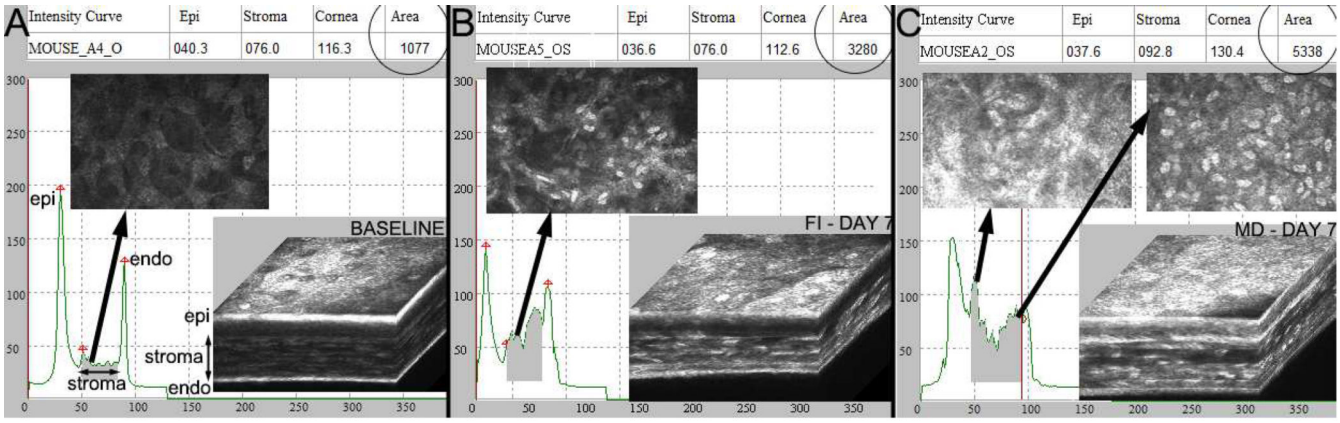

Figure 4.

In vivo CMTF data collected from mouse using the modified HRT-RCM system. A. Normal mouse cornea (C57/BL6). B. The wound healing response 7 days after transcorneal freeze injury (FI). C. The wound healing response 7 days after mechanical debridement (MD) injury with basement membrane removal. Mice were anesthetized using ketamine/xylazine for both procedures. For FI, a 1 mm diameter stainless steel probe cooled with liquid nitrogen was applied to the anterior, central corneal surface two times for 10 seconds each. For MD, the cornea was marked using a 2 mm diameter skin biopsy punch. The epithelium and basement membrane were then removed using an Algerbrush as previously described.[52] A relative estimate of stromal cell and ECM backscattering was obtained by measuring the area under the CMTF curve as previously described (shaded areas under curves, “area” on top right of each image). Note the increase in backscattering following injury.

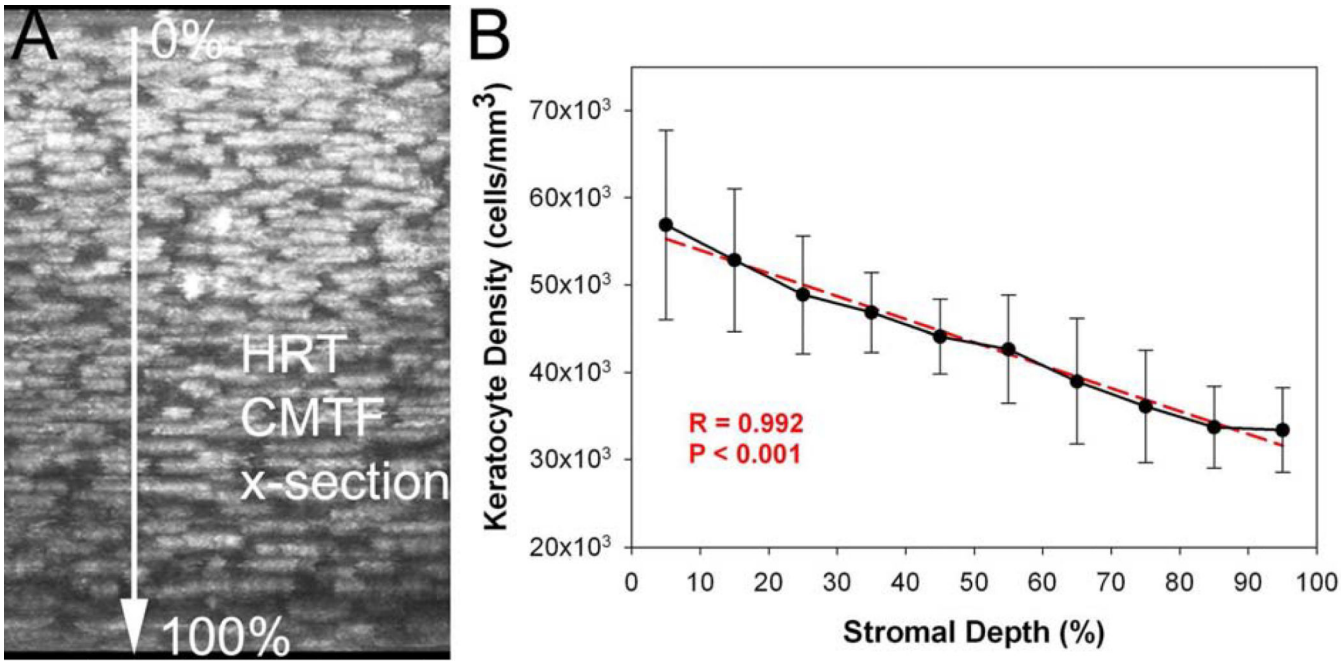

Figure 5.

A. Maximum Intensity Projection along the x-axis of an in vivo image stack collected using the CMTF program. B. Graph showing mean cell densities through the stromal thickness of six corneas. Both the image and the graph show progressively decreasing cell density through the stroma from the basal lamina to the endothelium. Graph shows mean and standard deviation of measurements from six corneas taken in vivo (N=6). (Reprinted with permission from Petroll WM, Weaver M, Vaidya S, et al. Quantitative 3-dimensional corneal imaging in vivo using a modified HRT-RCM confocal microscope. *Cornea* 2013;32:e36–43.)

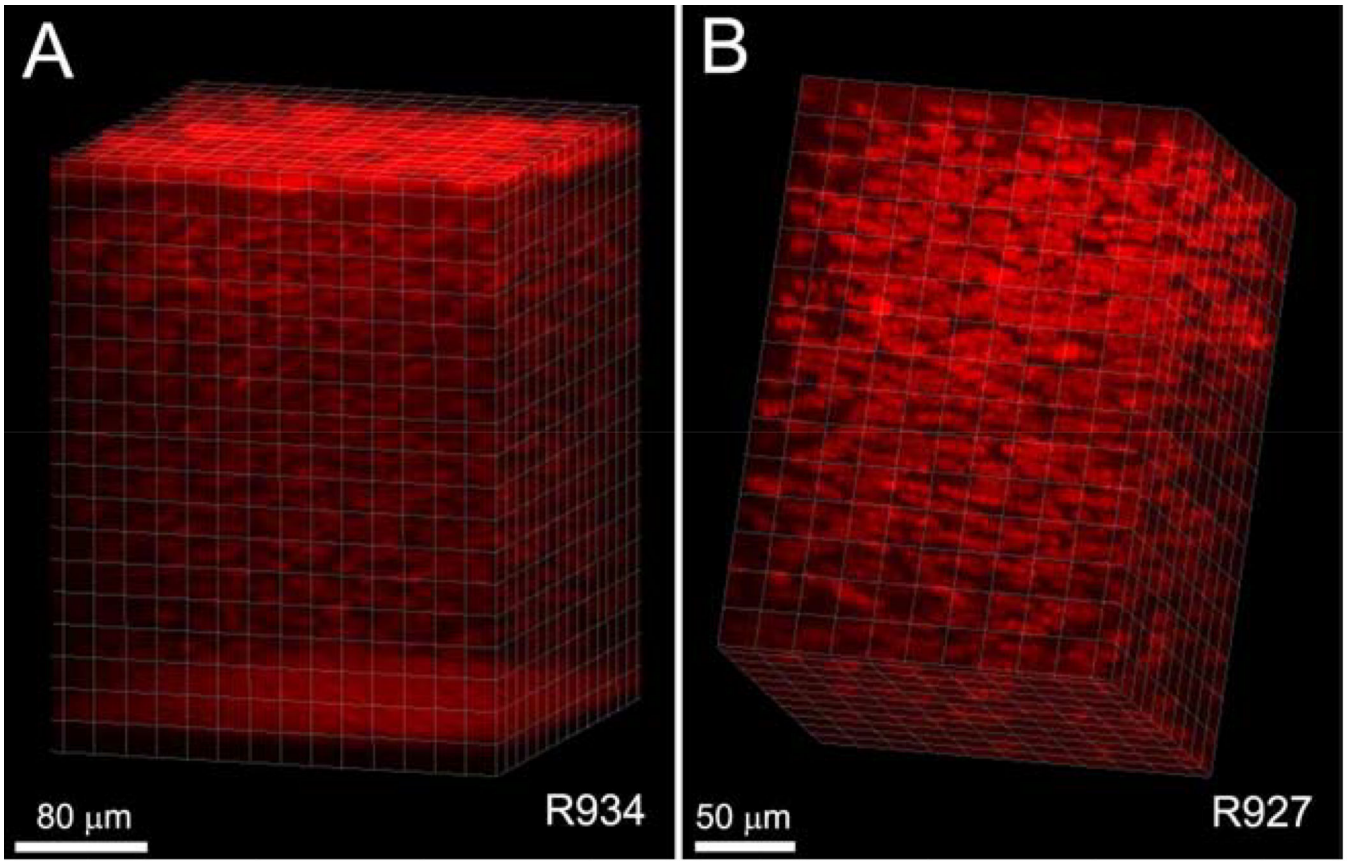

Figure 6.

Volume renderings of CMTF data from a rabbit cornea. Images were cropped in 3-D to focus on a region of interest, and rendered using an orthogonal maximum intensity projection within the *Surpass* module of Imaris. (Reprinted with permission from Petroll WM, Weaver M, Vaidya S, et al. Quantitative 3-dimensional corneal imaging in vivo using a modified HRT-RCM confocal microscope. *Cornea* 2013;32:e36–43.)

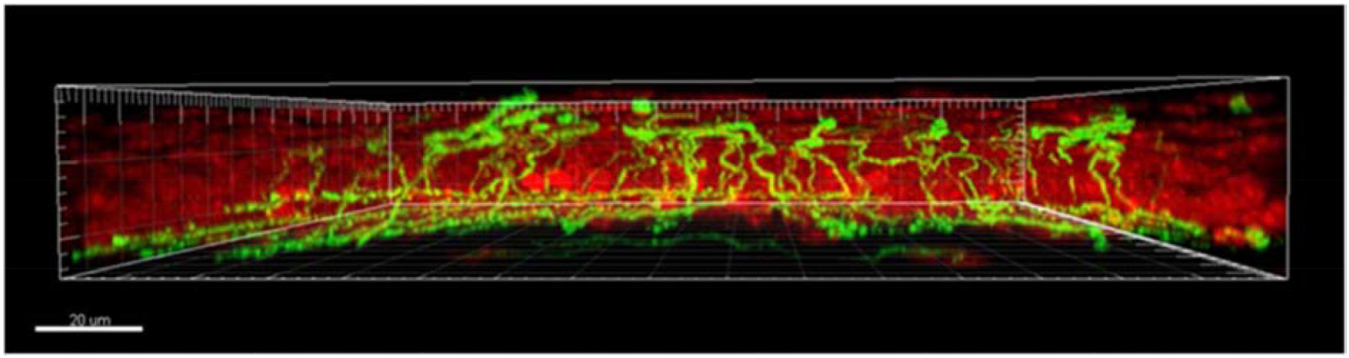

Figure 7.

Volumetric reconstruction of corneal epithelial nerves and the subbasal nerve plexus. Corneal nerves were stained with β tubulin (green). Epithelial nuclei were counter-stained with propidium iodide (red). Epithelial nerve fibers branching from the subbasal nerve plexus terminate among the superficial epithelial cells. Scale bar: 20 μm. (Reprinted with permission from Cai D, Zhu M, Petroll WM, et al. The impact of type 1 diabetes mellitus on corneal epithelial nerve morphology and the corneal epithelium. *Am J Pathol* 2014;184:2662-70.)

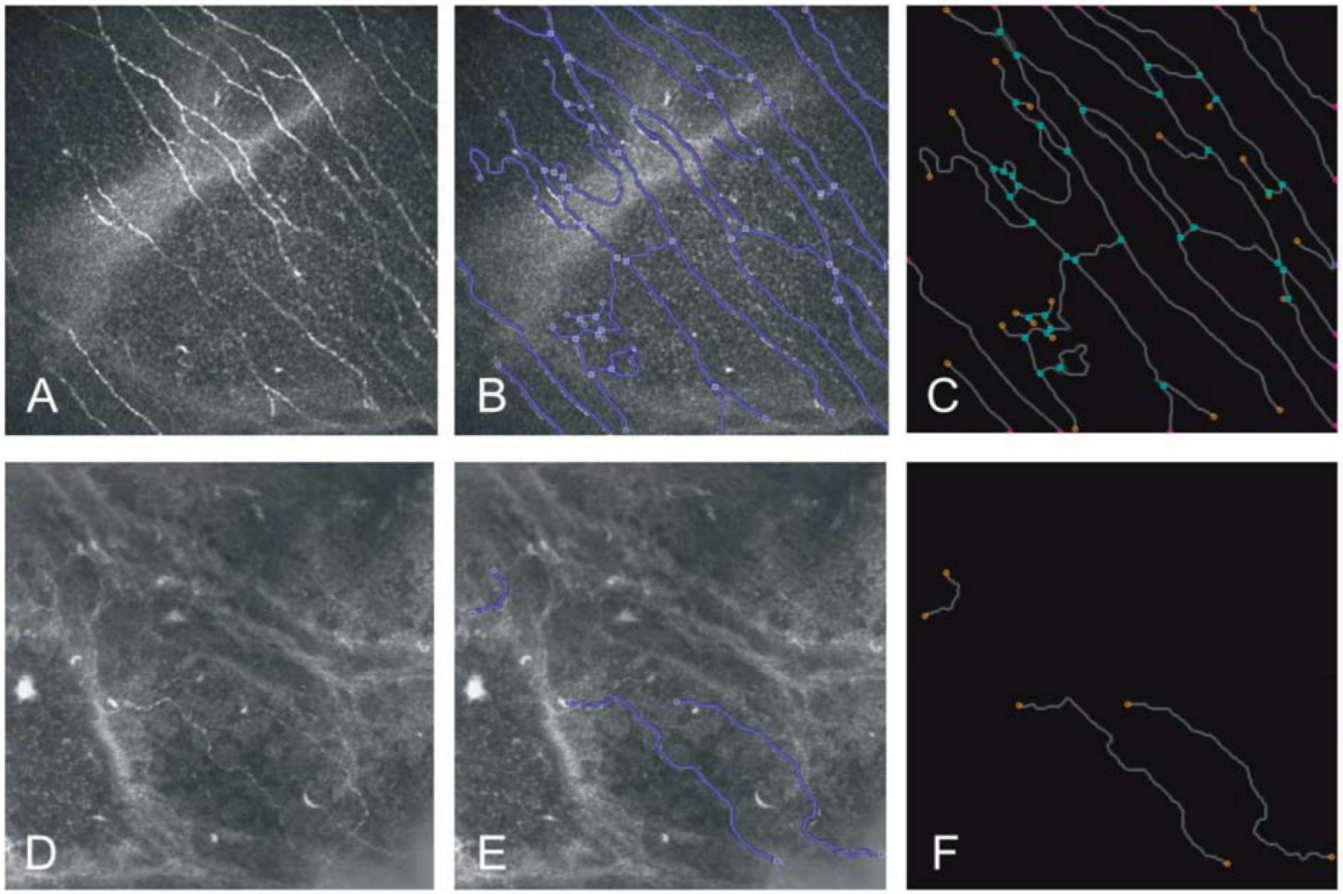

Figure 8.

Confocal microscopy and quantification of micromorphological parameters. Initial images of subbasal nerve plexus in the central cornea in a healthy volunteer (A) with corneal sensation 60 mm and diabetic patient (D) with corneal sensation 40 mm and NDS = 8 (image size: 400 × 400 μm). B and E represent the results of segmentation from the corresponding images in control and diabetic subjects, respectively. C and F show traces of the geometry of the subbasal nerve plexus in a final surface reconstruction. Total fiber length of 4706 and 545.4 μm, nerve fiber density 0.034 mm/mm^2 and 0.004 mm/mm^2, and single nerve fiber count 68 and 3 were measured in control subject and diabetic patient, respectively. (Reprinted with permission from Zhivov A, Winter K, Hovakimyan M, et al. Imaging and quantification of subbasal nerve plexus in healthy volunteers and diabetic patients with or without retinopathy. *PLoS ONE* 2013;8:e52157)

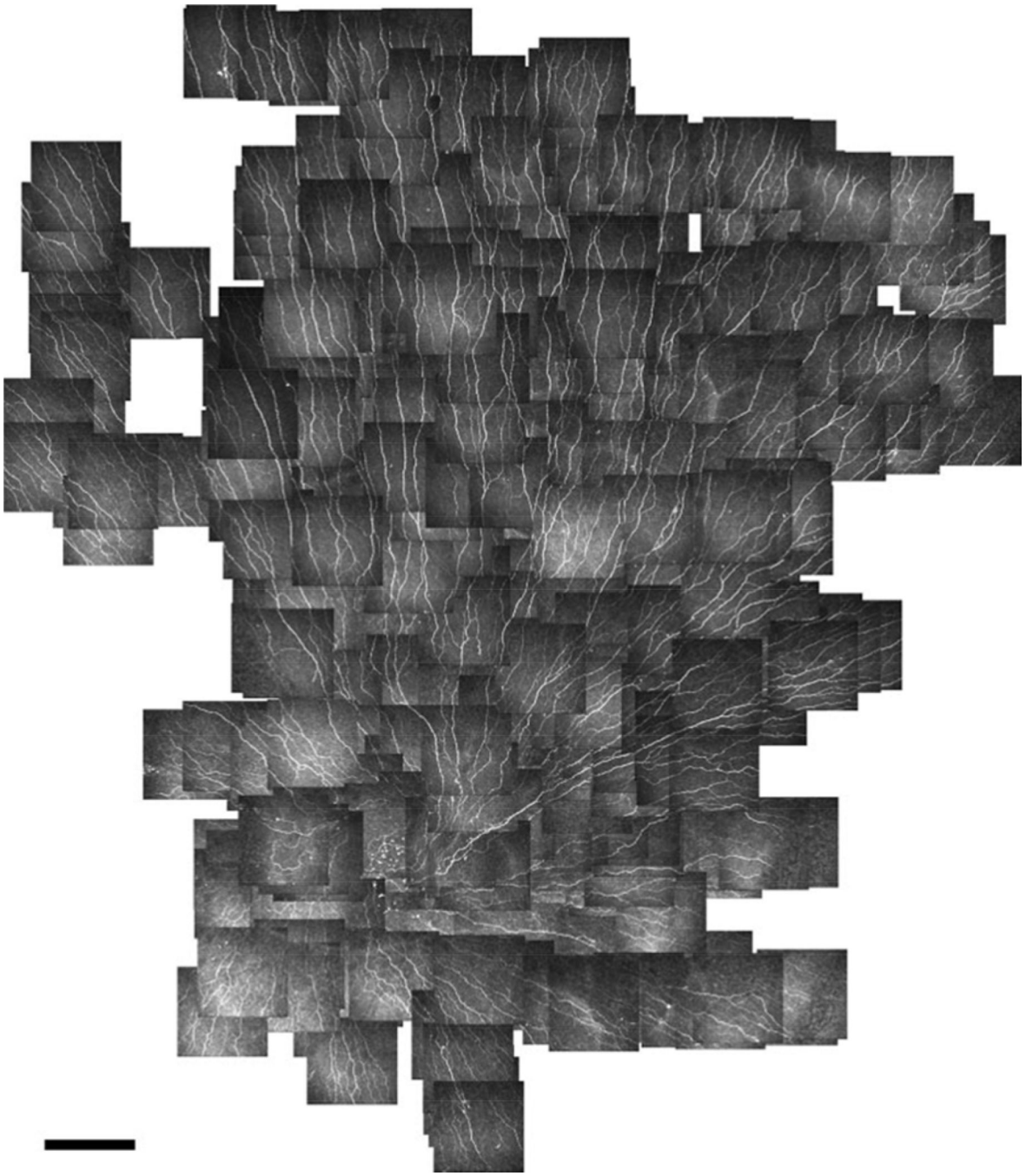

Figure 9.

Wide-field mapping of the subbasal nerve plexus. The first montage of the human subbasal nerve plexus reported by Patel and McGee. Scale bar: 400 μm. (Reprinted with permission from Patel DV, McGhee CN. Mapping of the normal human corneal sub-Basal nerve plexus by in vivo laser scanning confocal microscopy. *Invest Ophthalmol Vis Sci* 2005;46:4485-88.)

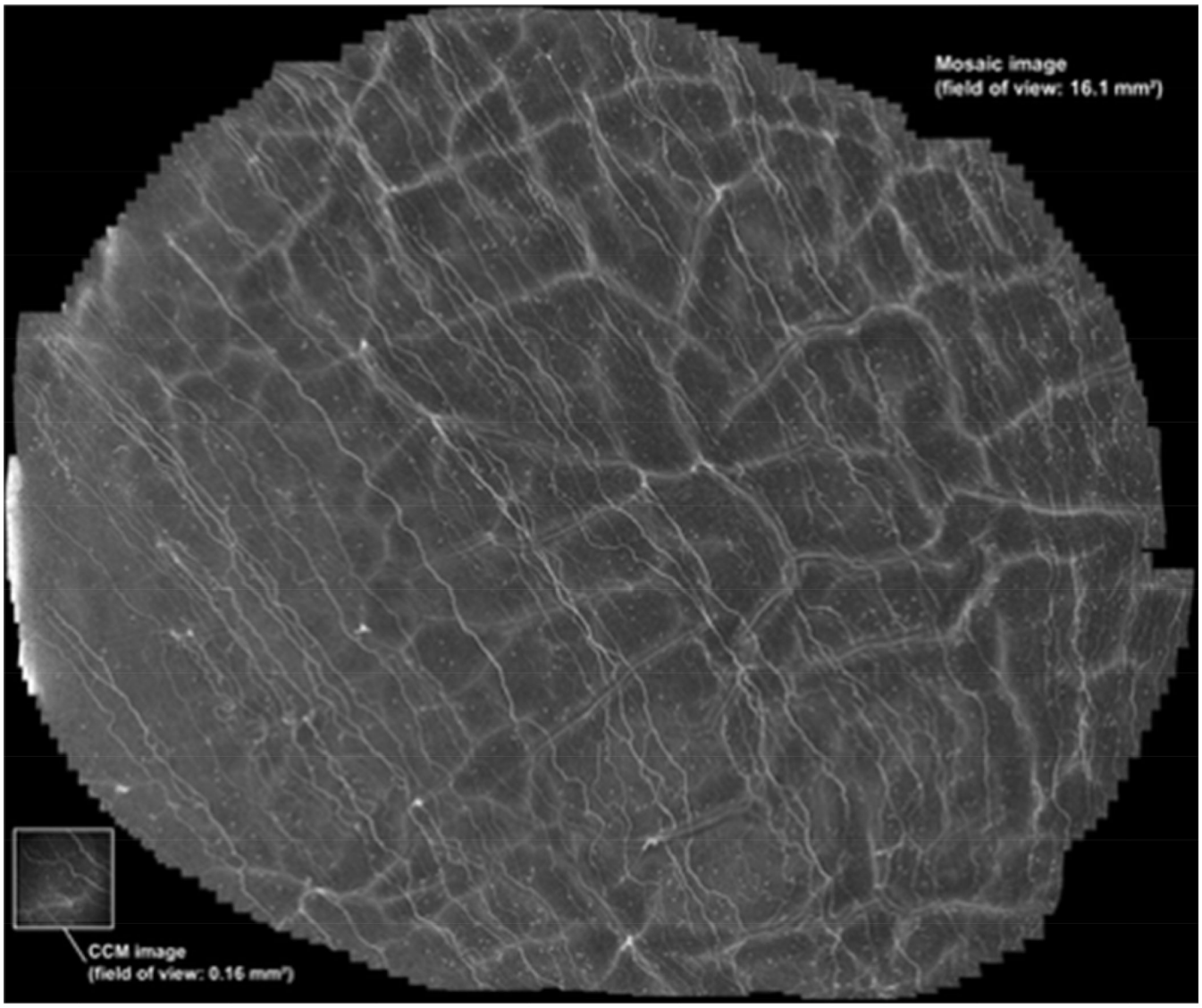

Figure 10.

Mosaic image generated by Allgeier. Using an outward spiraling fixation target, a wide-field map of the subbasal nerve plexus was generated 2541 processed images with a resultant field of view of 16.1 mm^2. (Reprinted with permission from Allgeier S, Maier S, Mikut R, et al. Mosaicking the subbasal nerve plexus by guided eye movements. *Invest Ophthalmol Vis Sci* 2014;55:6082-9.)

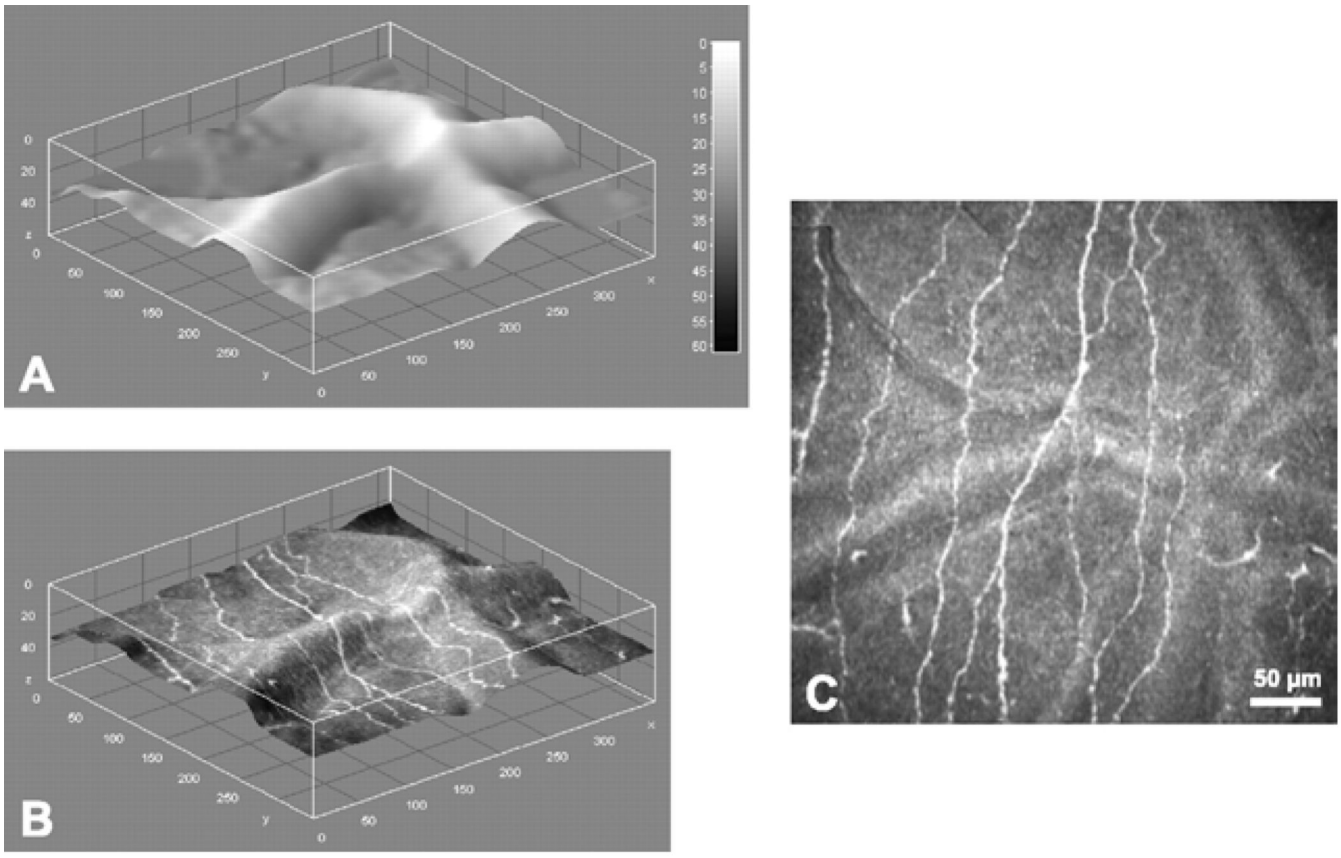

Figure 11.

Depth map and nerve fiber layer extraction at SNP level. A. Depth map of SNP layer inside the reconstructed volume. **B**. Depth map of SNP layer, textured with reconstructed image. **C**. Reconstructed image of the SNP. Image size: 362 × 347 pixels, 377 × 361 µm, ~85% of original image size. (Reprinted with permission from Allgeier S, Zhivov A, Eberle F, et al. Image reconstruction of the subbasal nerve plexus with in vivo confocal microscopy. *Invest Ophthalmol Vis Sci* 2011;52:5022-28.)